



Norwegian University of
Science and Technology

Studies of MUC1 - Gal3 lectin interaction by the sensitive force probe Optical Tweezers (OT)

Øystein Haug

Biotechnology

Submission date: May 2017

Supervisor: Marit Sletmoen, IBT

Norwegian University of Science and Technology
Department of Biotechnology and Food Science

*If we knew what it was we were
doing, it would not be called
research, would it?*

ALBERT EINSTEIN

Abstract

Aberrant glycosylation patterns of membrane-bound proteins have been observed to be a universal feature of malignant cells. Members of the mucin family of glycoproteins form one of the major carriers of aberrant glycosylation, where there in breast tissue cells and other carcinomas have been found an upregulation of the Mucin1 (MUC1) protein with an increase in several cancer-associated antigens such as the ST (α -Neu5Ac(2,3) β -Gal(1,3)-GalNAc-Ser/Thr), T (β -Gal(1,3)-GalNAc-Ser/Thr), Tn (GalNAc-Ser/Thr) and STn (α -Neu5Ac(2,6)-GalNAc-Ser/Thr) antigens. The presence of the different antigens are not fully understood, but an increase of sialic acid-glycostructures have been found in breast cancer cells.

The galactose binding family of lectins called galectins have been found to be present both extracellularly and intracellularly. A member of the β -galactose binding family, Galectin-3 (Gal3), have further been associated with processes such as acute inflammation as well as cancer increase and metastasis. Due to its important role in cancer development, the binding specificity of Gal3 is of interests. Gal3 have further been observed to interact with MUC1(T), but not with the MUC1(Tn). In a study published in 2007, interaction between MUC1(ST) and Gal3 was reported not to occur, but an unpublished study from London revealed informal information about a possibility of an interaction to occur.

The experimental data presented in this master thesis were recorded by using a dual beam setup of the sensitive force probe Optical Tweezers. The aim of this study was to provide new information concerning the interaction between the different MUC1-antigens and Gal3. The results obtained provide evidence that MUC1(ST) and Gal3 interact with a rupture strength of 11-31 pN when investigated using loading rates in the range of 39-72 pN/s. The energy landscape of the interactions gave a k_{off} -range from 1.3-2.9 s^{-1} and x_{β} -value of 0.54 nm. A rupture frequency analysis was included in order to estimate the occurrence of interaction. MUC1(ST) and Gal3 showed a main rupture frequency estimate of 42.8 % \pm 26. Parallel, interaction between the positive control MUC1(T) and Gal3 gave a rupture frequency estimate of 32.0 % \pm 16. The negative controls MUC1(Tn) and MUC1(Na) showed no specific interaction with Gal3.

A parallel study was performed by another masterstudent at NTNU, Ragna Emilie Bugge, where she also reported interaction between MUC1(ST) and Gal3 to occur by use of the sensitive force probe atomic force microscopy (AFM).

Sammendrag

Unormal glykosylering på membran-bundede proteiner er blitt observert som et vanlig trekk ved maligne celler. Medlemmer av mucin-familien av glykoproteiner er en av de største bærerne av unormal glykosylering, og Mucin 1(MUC1) er ofte oppregulert i brystkreftvev og carcinoma. Det er videre observert en økning i kreft-assosierte antigener som ST (α -Neu5Ac(2,3) β -Gal(1,3)-GalNAc-Ser/Thr), T (β -Gal(1,3)-GalNAc-Ser/Thr), Tn (GalNAc-Ser/Thr) og STn (α -Neu5Ac(2,6)-GalNAc-Ser/Thr). Tilstedeværelsen av de forskjellige antigenene er ikke fullt forstått, men en økt andelen sialinsyre er påvist på glykostrukturene til brystkreft celler.

Den galaktose-bindene familien av lektiner, kalt galektiner, er påvist både ekstracellulært og intracellulært. Et medlem av den β -galaktose bindende familien, Galektin-3 (Gal3), er assosiert med prosesser som akutt inflammasjon så vel som økning og metastase av kreftceller. På grunn av dens viktige rolle i utvikling av kreft, er bindingsspesifisiteten til Gal3 av interesse. Gal3 er videre blitt funnet å interagere med MUC1(T), men ikke med MUC1(Tn). I en studie publisert i 2007 ble det ikke funnet interaksjon mellom MUC1(ST) og Gal3, men data oppnådd i en upublisert studie fra London indikerer at det muligens skjer en interaksjon.

De eksperimentelle dataene i denne masteroppgaven ble tatt opp ved bruk av et dobbeltstråle-oppsatt av kraft proben Optical Tweezers. Hensikten med studiet var å oppnå ny informasjon om interaksjoner mellom MUC1-antigene og Gal3. Resultatene oppnådd viser at MUC1(ST) og Gal3 interagerer med en bruddstyrke på 11-31 pN ved undersøkelse i et loading rate-område på 39-72 pN/s. Energilandskapet til interaksjonene gav et k_{off} -område fra 1.3-2.9 s^{-1} og x_{β} -verdi på 0.54 nm. En bruddfrekvensanalyse ble utført i den hensikt å kunne anslå hyppigheten av interaksjoner. MUC1(ST) og Gal3 viste et bruddfrekvensestimat på 42.8 % \pm 26. Parallelt viste positivkontrollen MUC1(T) og Gal3 et bruddfrekvensestimat på 32.0 % \pm 16. Negativkontrollene MUC1(Tn) og MUC1(Na) viste ingen interaksjon med Gal3.

Et parallelt studium utført av en annen masterstudent ved NTNU, Ragna Emilie Bugge, har også rapportert om funn av interaksjon mellom MUC1(ST) og Gal3, ved bruk av den kraftsensitive proben atomær kraftmikroskopi (AFM).

Preface

This thesis is submitted to the Department of Biotechnology and Food Science at the Norwegian University of Science and Technology (NTNU), as a requirement for the Master of Science in Biotechnology. All the work was performed from January 2016 to June 2017 in the laboratories of Biophysics and Medical Technology at the Department of Physics, where one week of the period was used at the department of Research Oncology at King's College London. All figures in this master thesis are self-made in Inkscape, Matlab or Sigmaplot on the basis of cited theory, except of three figures who are achieved from JPK instruments.

First of all, I will forward a major credit and thanks to my primary supervisor, Associate Professor Marit Sletmoen at the Department of Biotechnology at NTNU, for recruiting me to this project. Her knowledge in the field of biochemistry, guidance, writing feedback and motivational speaks through the whole process has been essential for submitting this thesis.

Secondly, I wish to widen my thanks to Researcher Gianfranco Picco at department of Research Oncology at King's College London for being a huge encyclopedia and inspirer for me. His knowledge in the field of biology has been of great importance for understanding the main target with this thesis, including his feedback on my thesis. I will also thank him for inviting me to a one week visit at the department of Research Oncology at King's College London, allowing me to share my findings and absorb the knowledge present at the department. Thanks to Gianfranco Picco, I will be able to enjoy a delicious cup of fresh Italian brewed Moca-coffee as much as I want in the future.

I will also send a extended gratitude to Researcher Richard Beatson at the Peter Gorer Department of Immunobiology at Guy's Hospital for shearing his knowledge in the field of biology, even when the time did not make it possible. His perspective on the field of biology and his feedback on my thesis have helped me a lot in this process.

Additional, I will send a thanks to Professor Bjørn T. Stokke, for providing and maintenance the programs to analyse the interaction events, and Senior Engineer Gjertrud Maurstad for technical support during the experimental work.

At last, I will forward a thanks to master student Ragna Emilie Bugge for great collaboration, meaningful discussions and of course allowing me to include some of her results in my thesis.

Contents

Abstract	i
Sammendrag	iii
Preface	v
List of Tables	ix
List of Figures	xii
List of Abbreviations	xiii
1 Introduction	1
2 Background theory	3
2.1 Proteinsynthesis	4
2.1.1 mRNA translation	4
2.1.2 N-linked protein glycosylation	5
2.1.3 O-linked protein glycosylation	6
2.2 Mucins	7
2.2.1 MUC1	8
2.3 Lectins	10
2.3.1 Galectin-3	10
2.4 Oncogenic effects of MUC1-Gal3 interactions	11
2.4.1 Intracellular pathway	12
2.4.2 Metastasis	13
2.4.3 Downregulation of immuneresponse	14
3 Experimental theory	15
3.1 Optical tweezers	16
3.1.1 Optical trapping	17
3.1.2 Axial and lateral trapping	17
3.1.3 Calibration	19
3.1.4 Determination of intermolecular interaction forces using OT .	21
3.2 Dynamic force spectrum	22

3.2.1	Free energy landscape and the two state model	22
3.2.2	Calculations	24
3.3	Finding the rupture force and loading rate	27
3.3.1	iNanoTrackerOT3DPreProcess software	27
3.3.2	iNanoTrackerOT3DPostProcess software	28
4	Experimental Setup	31
4.1	Protein immobilization	32
4.1.1	PLL-PEG coating protocol	32
4.2	Quantification of intermolecular interactions	33
4.2.1	Preparation of the liquid cell	33
4.2.2	Optical settings and calibration	33
4.2.3	Parameter settings and analysing	34
4.3	Data processing	35
5	Results	37
5.1	MUC1(T) interacts with Gal3	38
5.2	MUC1(ST) interacts with Gal3	39
5.3	MUC1(Tn) and MUC1(Na) do not interact with Gal3	40
5.4	Rupture frequency	40
5.5	Non-exponentially increasing loading rate	42
5.6	DF-spectrum of MUC1(ST)-Gal3 interactions	42
5.6.1	Non-exponentially increasing loading rate affecting the DF-spectrum	45
6	Discussion	47
6.1	How does Gal3 interact with MUC1(ST)?	48
6.2	Biological consequences of MUC1-Gal3 interactions	50
6.3	Glycan specificity of Gal3	50
6.3.1	Interaction between MUC1(T) and Gal3	50
6.3.2	Negative control experiments	50
6.3.3	Interaction between MUC1(ST) and Gal3	51
6.4	Energy landscape of MUC1(ST)-Gal3 interaction	53
6.5	Rupture frequency analysis	54
6.6	Non-exponentially increasing loading rate	54
7	Conclusion	57
	Bibliography	59
	Appendix	I
A	ST, T and Tn-antigen structure conformations	III
B	Histogram results of MUC1(ST)-Gal3 interactions	V

List of Tables

5.1	Rupture frequency from all samples	41
5.2	Estimated parameters characterizing the energy landscape of MUC1(ST)-Gal3 interactions.	45

List of Figures

1.1	Glycan specific MUC1/Gal3 ELISA performed by Gianfranco Picco, King's College London	2
2.1	Illustration of protein N-glycosylation in rough-ER.	5
2.2	Illustration of O- and N-glycosylation.	7
2.3	MUC1-structure in normal cells and cancer cells	9
2.4	Gal3 monomer and pentamer structure	11
2.5	Comparison of the cell structure to normal cells and carcinoma cells.	12
2.6	Binding of Gal3 to MUC1 and RTK and activation of intracellular pathways in carcinoma cells	13
2.7	Illustration of MUC1-Gal3 induced lymphocyte T-cell apoptosis.	14
3.1	Illustration of OT instrument.	16
3.2	3D-model of the Gaussian distribution of a laser beam.	17
3.3	Illustration of axial and lateral trapping.	18
3.4	Back focal plane interferometry	19
3.5	Screenshot of OT-calibration.	21
3.6	Illustration of calculation steps in OT.	22
3.7	A simulation of how the free energy landscape is organized including a graphical illustration of the two state model.	23
3.8	Illustration of a DFS-plot for interaction forces between two molecules.	24
3.9	Simplified illustration of a DFS-plot for interaction forces between two molecules.	25
3.10	3D-illustration of the DFS-plot and the relationship between the DFS-plot and the Bell-Evans subgroups.	26
3.11	Print screen of interaction analysis in iNanoTrackerOT3DPreProcess program	28
3.12	Print screen of interaction analysis in the iNanoTrackerOT3DPostProcess program.	29
4.1	Liquid cell	33
4.2	Overview of the important steps performed in order to analyse in- teraction between MUC1 and Gal3 in OT.	34

5.1	Gallery and histogram presentation of MUC1(T)-Gal3 interactions. .	38
5.2	Gallery and histogram presentation of MUC1(ST)-Gal3 interactions.	39
5.3	Gallery presentation from some interaction-curves between the complex MUC1(Tn)-Gal3 and MUC1(Na)-Gal3.	40
5.4	A graphical presentation of the rupture frequency data	41
5.5	Examples of interaction curves with non-exponentially increasing loading rate	42
5.6	DF-spectrum for MUC1(ST) and Gal3 interactions.	43
5.8	Bell-Evans plots of the different subgroups from the DF-spectrum. .	44
5.9	Result of the mean trend to the DFS-plot.	44
5.10	Illustration of the results of non-exponentially increasing loading rate affecting the DF-spectrum.	46
6.1	ST, T and Tn-antigen structure conformations.	48
6.2	Illustration of some binding abilities present in ST-Gal3 interactions	49
6.3	Combined DF-spectrum for MUC1(ST) and Gal3 interactions measured in AFM and OT.	52
A.1	ST, T and Tn-antigen structure conformations.	III
B.1	DF-spectrum for MUC1(ST) and Gal3 interactions.	V
B.2	Bell-Evans plots of subgroup 1-6 from the DF-spectrum.	VI
B.3	Bell-Evans plots of subgroup 7-10 from the DF-spectrum.	VII

List of Abbreviations

Abbreviations	Description
AFM	Atomic force microscopy
Asn	Asparagine
Dol	Dolichol
EGFR	Epidermal growth factor receptor
ER	Endoplasmic reticulum
Gal3	Galectin-3
GalNAc	N-Acetylgalactosamine
GlcNAc	N-Acetylglucosamine
LacNAc	N-Acetylglactosamine
LBG	Large binding groove
MUC1	Mucin 1
Neu5Ac	N-Acetylneuraminic acid
OST	Oligosaccharyl transferase
OT	Optical Tweezers
Pro	Proline
QPD	Quadrant photodiode
RTK	Receptor tyrosine kinase
SEA	Sea-urchin sperm protein, Enterokinase and Agrin
Ser	Serine
ST	α -Neu5Ac(2,3) β -Gal(1,3)-GalNAc-Ser/Thr
STn	α -Neu5Ac(2,6)-GalNAc-Ser/Thr
T	β -Gal(1,3)-GalNAc-Ser/Thr
Thr	Theronine
Tn	GalNAc-Ser/Thr

Chapter 1

Introduction

In 2012, malignant cancer was the primary cause for the deaths of 8.2 million people worldwide (Chia, Goh, & Bard, 2016). A universal feature of human cancer cells is that they present an aberrant glycosylation pattern, where changes in Ser/Thr O-glycosylation result in several cancer-associated antigens (Ono & Hakomori, 2003). Different glycoproteins including the mucin1 (MUC1) have shown to present such antigens. Furthermore the presence of such antigens on MUC1 have been reported to be essential for the interaction with different lectins. The interaction between MUC1 and lectins such as Galectin-3 (Gal3) is known to play an important role for the existence and metastasis of cancer cells (Beatson et al., 2015). MUC1-antigens such as T (β -Gal(1,3)-GalNAc-Ser/Thr) have been reported to interact with Gal3 (Zhao et al., 2010), whereas there are indications that another Core-1 antigen, the Tn (GalNAc-Ser/Thr)-antigen, does not interact with Gal3 (Iurisci et al., 2000).

The ST (α -Neu5Ac(2,3) β -Gal(1,3)-GalNAc-Ser/Thr)-antigen, has been reported not to interact with Gal3 (Yu et al., 2007). However unpublished data obtained by Gianfranco Picco at King's College London showed interactions between MUC1(ST) and Gal3 to occur. These data included a glycan specific MUC1/Gal3 ELISA test and are reproduced in figure 1.1 with his permission. In these previous studies the interactions were investigated at a cellular level. The aim of this master thesis is to investigate the ability of MUC1(ST) and MUC1(T) to interact with Gal3 at a molecular level, and also to shed light on the properties of these glycan-lectin interactions.

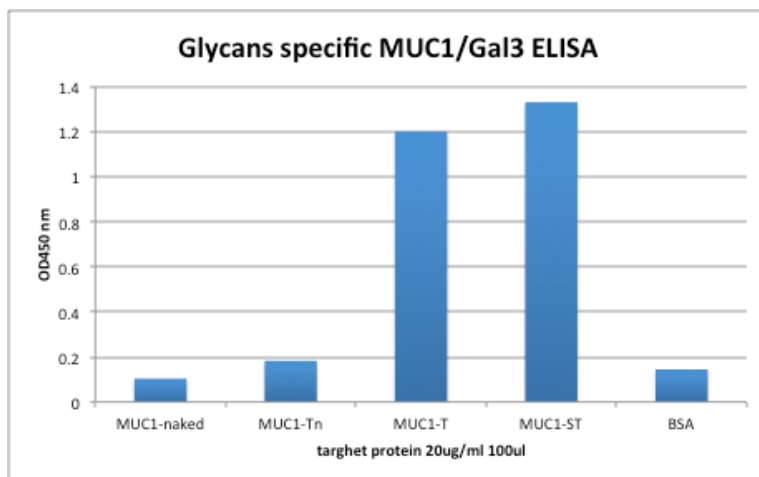


Figure 1.1: Glycan specific MUC1/Gal3 ELISA performed by Gianfranco Picco, King's College London. Recombinant MUC1 glycoproteins expressing predominantly either no O-linked glycans or the glycan Tn, T or ST were used as target protein by coating ELISA plates with 2 μ g of proteins, before blocking with BSA, Gal3 binding and colorimetric visualization. Reproduced with permission from Gianfranco Picco, King's College London.

Chapter 2

Background theory

One of the most complex post-translational modifications of proteins is glycosylation. This chapter will give a brief introduction to protein synthesis, the general mechanisms behind protein glycosylation and the difference between various types of glycosylation processes. Information about the glyco-protein MUC1 and the lectin Gal3 are also presented, and the chapter rounds off with a section on how interaction between MUC1 and Gal3 can play a key role in cancer progression including metastasis.

2.1 Proteinsynthesis

Each cell displays several types of membrane-bound proteins which possesses several functions within the cell or related to its interaction with the extracellular space. In order to produce specific proteins with specific functions, each protein is produced, folded and glycosylated by different mechanisms in the cell. First, the protein-coding DNA-sequence is transcribed to messenger-RNA (mRNA). The intron sites are then removed and the mRNA coiled and capped at its 5'end. Different transport proteins transport the mRNA-sequence from the nucleus to the cytosol where it undergoes mRNA-translation (Alberts, Wilson, & Hunt, 2015).

2.1.1 mRNA translation

Translation is the process where the mRNA attaches to a ribosome at the small ribosomal subunit. A ribosome consist of a small and a large subunit with three mRNA binding sites called E-, P-, and A-site. The growing polypeptide chain is always attached to the transfer-RNA (tRNA) at the P-site, where the A-site is the first bindingsite of a tRNA with one specific amino acid attached. Each tRNA has a triplet-codon, consisting of three mRNA-nucleotide bases, which code for a specific amino acid that is attached. During translation a tRNA with corresponding triplet-codon to the mRNA-sequence binds at the A-site, which change the binding site from the A-site to the P-site. This induces the transfer of the attached amino acid to the growing polypeptide chain. The growing polypeptide chain is continuously folded at the N-terminal domain. The folding of the C-terminal domain is completed at the end of translation, where the protein is finally completed after the glycosylation-process in endoplasmic reticulum (ER) (Alberts et al., 2015, p.299-365).

During translation of the mRNA-sequence that code for a transmembrane protein, the first amino acids that are synthesized constitute a start-transfer sequence. A signal recognition particle (SRP) binds to the start-transfer sequence which then attaches to a SRP-receptor at the rough ER-membrane. The SRP is then released and transferred to an protein translocation channel in the ER. Parallel to translation, the growing polypeptide chain is partly released through the translocation channel and into the ER-lumen. The release process stops when a stop-transfer sequence reaches the translocation channel. This sequence consists of hydrophobic amino acids and the protein will then, because of the hydrophobic lipid layer in the

ER-membrane, smoothly slide out of the translocation channel and become part of the ER-membrane (Alberts et al., 2015, p.669-681).

2.1.2 N-linked protein glycosylation

N-glycosylation is a the glycosylation process that starts in the ER-lumen during mRNA translation. The N-glycosylation starts when the protein has partly completed its translation and taken place in the ER-membrane. A "precursor oligosaccharide", consisting of 2 N-acetylglucosamine, 9 mannose- and 3 glucose-molecules is anchored to a membrane bound protein called dolichol. The hydrogen molecule in the polypeptide side chain Asparagine (Asn) can be replaced by binding to the "precursor oligosaccharide", where binding to the NH_2 -group in Asn is called N-linked glycosylation or "N-glycosylation". Initiated by oligosaccharyl transferase and production of Asn, the "precursor oligosaccharide" is transferred from dolichol to the growing polypeptide. Figure 2.1 illustrates the mRNA-translation by the ribosome on the rough ER-surface, the attachment of the polypeptide chain to the translocation channel, and the N-linking of the "precursor oligosaccharide" to Asn by oligosaccharyl transferase (Alberts et al., 2015, p.673-687).

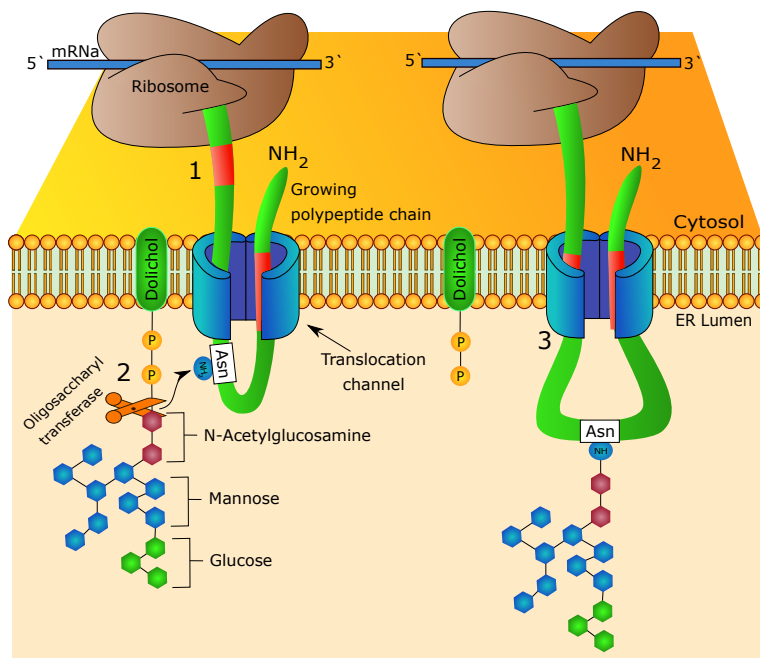


Figure 2.1: Illustration of protein N-glycosylation in rough-ER. (1) The mRNA-sequence is translated by the ribosomes on the rough-ER membrane. The growing polypeptide chain is transported to the translocation channel, where the two red fragments in the polypeptide chain codes for a hydrophobic start- and stop-transfer sequence. (2) When a Asn-amino acid is produced, the "precursor oligosaccharide" is detached from the dolichol-diphosphor group and attached to the NH_2 -group in Asn by oligosaccharyl transferase. (3) When the stop-transfer sequence is produced, the hydrophobic start- and stop-transfer sequence will slide out of the translocation channel and take place in the ER-membrane.

Due to the fact that glycosylation can interfere with protein folding, the amino acid Asn occur less frequently in glycoproteins than in nonglycosylated proteins. The function of this "*precursor oligosaccharide*" is to control the protein folding of N-glycans, where a glycosyl transferase control if the protein is completely folded. Glucose trimming is performed at the precursor oligosaccharide and then bind to a ER-membrane bound protein called calnexin. If the protein is completely folded and ready to be exported out of the ER, the glucosidase does another glucose trimming, releasing the glycoprotein from calnexin. If the protein is incompletely folded, glycosyl transferase will bind to it and initiate addition of a new glucose which then again will bind to calnexin. The process repeats until the protein is completely folded. Misfolded proteins will be exported and degraded in the cytosol (Alberts et al., 2015, p.673-687).

Export of the glucoprotein go through vesicle transport from ER to the golgi apparatus. Golgi apparatus is the main distributor in vesicle transport, but is also important in carbohydrate synthesis. In the golgi lumen, the oligosaccharide on the glycoprotein goes through further modification. When the membrane glycoprotein is completely modified through cis cisterna, medial cisterna and trans cisterna in the golgi apparatus, specific receptors bind to the complex oligosaccharide and transport the glycoprotein through vesicles. The vesicle containing the membrane protein is then transported to the cell membrane and melt together with the plasma membrane by exocytosis. The membrane protein are then flipped, facing out of the cell to the extracellular space (Alberts et al., 2015, p.717-742).

2.1.3 O-linked protein glycosylation

As described in the previous section, the N-linked glycosylation is attached to the NH_2 -group in Asn. The final N-linked glycans are found to be of more than 500 different N-linked glycan structures, and can be classified into three main groups: high-mannose N-glycan, complex N-glycan or hybrid N-glycan. Another protein glycosylation process is called O-linked protein glycosylation or O-glycosylation, and occur first in golgi. Where the N-glycans are termed after attachment to the NH_2 -group in Asn, the O-glycans are termed after attachment to the OH-group in Ser(serine) or Thr(threonine). During the glycosylation steps of O-glycans in golgi, the different monosaccharides are stepwise added onto the Ser/Thr-side chains, where the N-glycans experience a stepwise removal of monosaccharides through the golgi. Due to the change in glycosylation pattern, the O-glycans are larger and more complex than the N-glycans (Preston, Rawley, Gleeson, & O'Donnell, 2013). The different O-linked glycans have several core-structures e.g. Core-1, Core-2, Core-3, but they all have the same GalNAc(N-acetylgalactosamine)-structure O-linked to the Ser/Thr. O-glycans can also be O-mannose, O-fucose and O-glucose (Marth & Grewal, 2008). The O-glycans can be grouped into two main groups: long O-glycans and short O-glycans. Figure 2.2 illustrate some structural differences between N-glycans and O-glycans found on membrane-bound proteins, and their attachment to OH- or NH_2 -groups at Ser/Thr or Asn. This thesis will focus on different glycan structures within the short O-glycan group, which has been observed to affect tumor development (Chia et al., 2016).

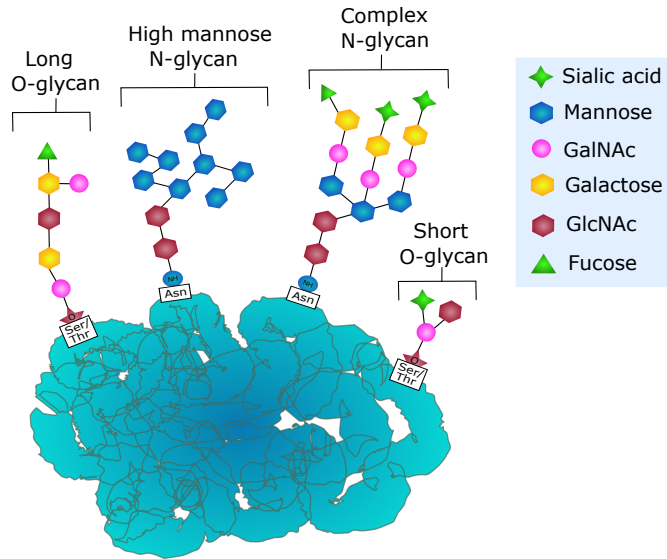


Figure 2.2: Illustration of some of the different groups of O- and N-glycans found on membrane-bound proteins. The O-glycans are primarily found to have GalNAc as core-monosaccharide, where N-glycans primarily have a GlcNAc-GlcNAc-Mannose core-structure. The N-glycans can be found as high mannose N-glycans or complex N-glycans, but the structure vary. O-glycans can be found as long O-glycans or short O-glycans, but the structure vary.

2.2 Mucins

Mucins are found in the intestine, lungs, breasts, kidneys, pancreas, gall bladder and gastric glands, and are important components of the protective mucous layer on the epithelial surface of the gut and ductules. The functions of mucins vary, but many mucins are involved in forming a protective mucose barrier, cell-surface signalling and/or control of the local microenvironment surrounding the cells. Several tumor-associated antigens have been identified on mucins, including the CA125 antigen that is associated with ovarian carcinomas [(Hollingsworth & Swanson, 2004), (Corfield, 2015)].

The amino acid backbones of mucins are up to hundred of nanometers long, build up by a various number of variable number tandem repeat (VNTRs) and can have around 5–100 potential glycosylation sites per repeat. The range in molecular weight of each mucin varies from 50-240 kDa. About 50–80% of the glycans are O-linked to Ser or Thr, where the remaining portion are N-linked (Hollingsworth & Swanson, 2004).

The different mucins all have a glycosylated transmembrane domain and an extracellular domain, but are grouped into three subgroups based on their functions: gel forming secreted mucins, non-gel forming secreted mucins and membrane-associated mucins. The secreted mucins that are gel forming e.g. MUC2, found in jejunum, ileum, colon and endometrium, consist of a cysteine-knot domain which shows homology to von Willebrand factor. This factor is known as an important

glycoprotein involved in hemostasis. The cystein-knot domain has a similar function for the mucin, where it alters gel-forming properties, an important function in order to create a protective mucosal barrier outside the tissue [(Hollingsworth & Swanson, 2004), (Corfield, 2015)]. MUC8 can be mentioned as a non-gel forming secreted mucin, found in eg. uterus, endocervix and the respiratory tract. The membrane-associated mucins e.g. MUC1, found on several epithelial cells in e.g. breast, colon and trachea, do not form gels but present a wide spectrum of glycans that can interact with the extracellular environment. The MUC1-glycans have further shown to be changed in carcinomas (Burchell, Mungul, & Taylor-Papadimitriou, 2001), where the altered glycosylation has an important impact on cancer progression (Kufe, 2010).

2.2.1 MUC1

MUC1 is a multifunctional transmembrane glycoprotein that is found on epithelial cells in lung tissue, abdomen, small intestine and breasts. The protein has been shown to be involved in signal transduction, protection of different mucus membranes, and modulation of the immune system. The genetic information of the protein is found on chromosome 1 (1q21) (Corfield, 2015). MUC1 has a molecular weight of over 400 kDa, and is a major component of the cell surface of glandular cells, meaning cells that produce secretion (Schwab, 2012)[p.256-258].

MUC1 is a heterodimer, consisting of an extracellular subunit (MUC1-N) and a transmembrane subunit (MUC1-C) as illustrated in figure 2.3 (Kufe, 2010). The N-terminal subunit consist of 20 tandem repeats (TR)-regions where each TR has 9 glycosylation sites. At the end of the N-terminal subunit, a sea-urchin sperm protein, enterokinase and agrin (SEA)-domain is attached which is found on several O-glycosylated cell-surface-associated proteins (Hollingsworth & Swanson, 2004). The SEA-domain is found to assist or to regulate the proteins ability to bind glycans, but is primarily an structural glycosylated domain (Mbanefo et al., 2014). The C-terminal subunit primary functions as a transmembrane receptor, and has an intracellular cytoplasmic tail, a transmembrane component and an extracellular SEA-domain. The extracellular part of MUC1-C is found on the apical surface and consists of 58 amino acids (Kufe, 2010). MUC1 also consists of a proteolytic cleavage site (PC-site) that is localized between the two SEA-domains in the N-terminal domain and the C-terminal domain (Hollingsworth & Swanson, 2004).

MUC1 molecules are heavily and randomly glycosylated in normal cells, but in case of cancer cells the glycosylation pattern is changed from elongated Core-2 structures to short Core-1 structures (Burchell et al., 2001). The cancer cells are shown to mainly express four types of Core-1 Ser/Thr O-linked cancer associated antigen structures such as; ST (α -Neu5Ac(2,3) β -Gal(1,3)-GalNAc-Ser/Thr), T (β -Gal(1,3)-GalNAc-Ser/Thr), Tn (GalNAc-Ser/Thr) and STn(α -Neu5Ac(2,6)-GalNAc-Ser/Thr). Figure 2.3 illustrates the change in glycosylation pattern for normal cells illustrated with a random glycosylation pattern and cancer cells, illustrated with an ST antigen structure. The T and Tn antigen structures have been shown to trigger immune response, where the STn-structure has shown to increase cell migration and decrease cell growth (Brockhausen, 2006). Expression

of short O-glycan groups has been observed to affect tumor development (Chia et al., 2016), where the O-glycan groups Core-1 and Core-2 was shown to be correlated with metastasis and prostate cancer progression in mice [(Moriyama, Nakano, Igawa, & Nihira, 1987), (Hagisawa et al., 2005)]. Loss of Core-1 O-glycans have further been observed to decrease development of breast cancer in mice (Song et al., 2015), which indicates the glycan structures to be of important therapeutic interest.

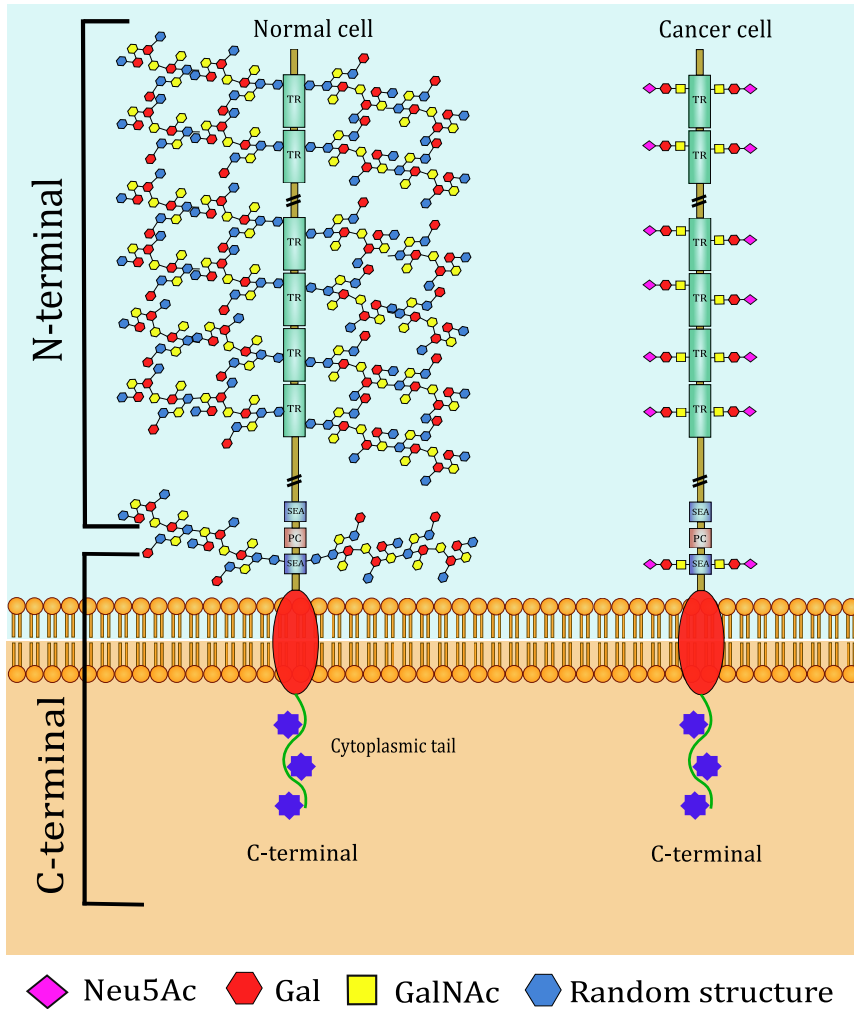


Figure 2.3: Illustration of the MUC1-structure in normal cells and cancer cells with the change in glycosylation pattern. The MUC1-structure consists of a N-terminal, a PC-domain and a C-terminal subunit. The N-terminal subunit consists of several heavily glycosylated TR-regions and a SEA-domain. The C-terminal subunit consists of an extracellular SEA-domain, a transmembrane domain and an intracellular cytoplasmic tail.

2.3 Lectins

Lectins are structurally diverse proteins found in animals, plants, microorganisms and viruses, and with a characteristic property of binding to carbohydrates. The majority of lectins recognize the most important monosaccharides that are present on the cell-surfaces, e.g. mannose, glucose, galactose, N-Acetylglucosamine (GlcNAc), N-Acetylgalactosamine (GalNAc), fucose and N-Acetylneuraminic acid (Neu5Ac). The proteins are oligomeric which means that several of them are composed of more than one subunit, in this case polypeptide chain. In general, each lectin molecule has at least two carbohydrate binding sites which give the lectin the possibility to cross-link, agglutinate and precipitate cells. This activity is similar to antibodies but differ in the manner of creating immune response. Lectins also have several similarities with enzymes, but lack the important catalytic activity site that enzymes contain (Sharon & Lis, 2007, p.1-2).

Galectins, one of the most commonly found animal lectins beside C-type lectin and siglecs, are characterized by their specific binding affinity to β -galactose. They are found in a variety of cell types, including fibroblast, ovary cells, dendritic cells, macrophages, T- and B-cells and endothelial cells (Klyosov, Witczak, & Platt, 2008), and are about 14-35 kDa large (Sharon & Lis, 2007, p.132-135). In general, their affinity to various glycans differ between different types of galectins, but they all have high affinity for N-Acetylglucosamine (GlcNAc). Further, Galectin-10 (Gal10) binds mannose and Gal3 binds different non-lactose sugars. Most of the proteins in the Galectin family operate as a "prototype" with only a single-carbohydrate recognition domain (S-CRD), or as a "tandem" with multiple CRD-regions and a linker with about 70 amino acids. For the S-CRD group, the CRD is required for their carbohydrate recognition activity, where a ligand binding groove (LBG) defines their binding specificity. Galectins have an highly conserved structure and are found extracellularly and intracellularly. The proteins are further involved in several biological processes such as inflammation response, cellular communication, immune regulation, and cellular growth and differentiation (Di Lella et al., 2011).

2.3.1 Galectin-3

Galectin-3 (Gal3) is found both extracellularly and intracellularly, and is a member of the β -galactose binding family of lectins called galactins. It is found to be involved in several processes including promotion of acute inflammation, promotion of cytokine secretion, favouring differentiation of β -cells and mediate the microenvironment to different types of malignant tumors. Further, poor survival prognosis for leukemia, lymphomas, breast cancer and thyroid cancer have been reported where increased level of Gal3 has been seen (Ruvolo, 2015).

The Gal3 is a 29–35 kDa "chimeric" lectin and consist of a S-CRD monomer, a collagen-like domain and a short N-terminal domain. The collagen-like domain is formed by several Pro-Gly-Tyr amino acid-tandem repeats (Fortuna-Costa, Gomes, Kozlowski, Stelling, & Pavão, 2014). Gal3 occurs mainly as a monomer in cytosol, but can travel through membranes to reach extracellular space, nucleus and mito-

chondria. The secretion of Gal3 to the extracellular environment is independent of the ER-golgi complex due to the lack of a signal peptide. The secretion pathway of Gal3 was suggested to be via exosomes (Mehul & Hughes, 1997), where the N-terminal domain further have been pointed out to be of importance as a signalling factor in the manner of secretion (Menon & Hughes, 1999). After secretion, Gal3 can bind to cell-surface-glycoproteins and form a pentamer constitution, which consists of five Gal3 monomers that are linked together through each N-terminal domain. Figure 2.4 illustrates the monomer and pentamer form of Gal3. This ability to form pentamers enables Gal3 to mediate cross-linking of other glycoproteins. Such cross-linking induces the signalling effect of activated glycoproteins, eg. activated epidermal growth factor receptor (EGFR) (Fortuna-Costa et al., 2014).

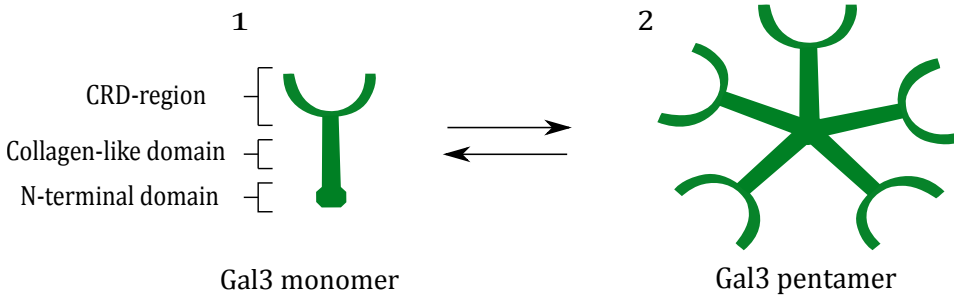


Figure 2.4: (1) Illustration of the Gal3 structure with its recognition domain, collagen-like domain and N-terminal domain. (2) Gal3 pentamer constitution where five Gal3 monomers are connected through each N-terminal domain (Fortuna-Costa et al., 2014).

2.4 Oncogenic effects of MUC1-Gal3 interactions

MUC1 and Gal3 separately have important roles for the cell in order to control the extracellular microenvironment and regulate cellular growth. As described, MUC1 consists of a backbone with several highly O-glycosylated TR-region. Parallel to the MUC1-structure, Gal3 has high affinity to several glycans such as LacNAc and non-lactose sugars found on the TR-regions of MUC1. In malignant tumors, MUC1 and Gal3 are both overexpressed and have been reported to interact. Further, the mentioned increase in Core-1 antigens on MUC1 in carcinoma cells leads to different binding abilities for Gal3. Studies have reported Gal3 to bind the T-antigen, also denoted as TF (Thomsen–Friedenreich)-antigen (Yu, 2007), which is reported to be present in 90% of all human carcinomas [(Mori et al., 2015), (Yu et al., 2007)]. There are indications that another Core-1 antigen, the Tn-antigen, does not interact with Gal3 (Iurisci et al., 2000). Further, one study has investigated binding of ST-antigen and Gal3 where no interaction was observed with the sialic acid attached (Yu et al., 2007).

Investigation of interactions between Gal3 and MUC1 have indicated several cancer-associated events such as activation of intracellular pathways, induced metastasis and downregulation of immunerespons by T-cell apoptotis [(Kufe, 2010), (Xin, Dong, & Guo, 2015), (Fukumori et al., 2003)].

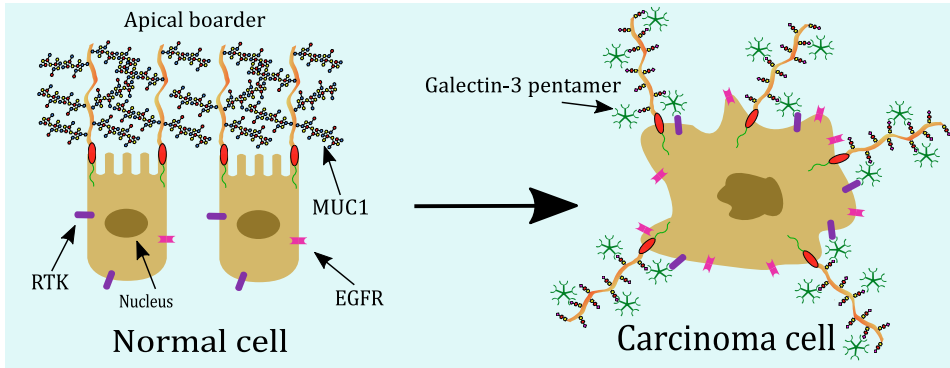


Figure 2.5: Comparison of the cell structure to normal cells and carcinoma cells. Normally O-glycosylated MUC1 is expressed on the apical border in normal cells, with RTK and EGFR expressed between the cells. In carcinoma cells, expression of MUC1, RTK and EGFR is increased and become random placed. Loss of polarity gives Gal3 the opportunity to bind to MUC1 between RTK and MUC1, which then activate intracellular pathways (Kufe, 2010).

2.4.1 Intracellular pathway

A normal cell has several highly O-glycosylated MUC1-proteins bound to the apical border of the cell membrane. Receptor tyrosine kinase (RTK) and epidermal growth factor receptor (EGFR) are some cell-membrane proteins that are normally not located on the apical border, but between the cells. Figure 2.5 illustrates the position of the apical border and localization of the MUC1-, EGFR- and RTK-proteins. A carcinoma cell undergoes a change in polarity and is further characterised by an increased level of MUC1, RTK and EGFR. Due to both loss of polarity to the apical border of the cancer cell and Gal3 pentamer formation, Gal3 can bind to the RTK and the O-glycans on the C-domain of MUC1 simultaneously as a signalling bridge. MUC1 is not able to phosphorylate and activate intracellular pathways when binding to Gal3, but by binding to both MUC1 and RTK, Gal3 is able to activate RTK to phosphorylate the intracellular tail of the MUC1-C domain. Activation of RTK phosphorylates the YEKV- polypeptide sequence of the intracellular cytoplasmic tail of the MUC1-C domain (illustrated in fig.2.3), which further induces the following SAGNGGSSLS-polypeptide sequence to bind β -catenin (Kufe, 2010). The intracellular tail of MUC1 has been reported to have 7 conserved tyrosine residues that each can be phosphorylated by RTK. Parallel, EGFR has been reported not to effect the MUC1-mediated signalling events (Mori et al., 2015). Phosphorylation of the MUC1-tail induces cleavage and oligomerization at the CQC-polypeptide sequence of the cytoplasmic tail. The CQC-polypeptide sequence is then targeted and transported to the nucleus by importin- β . The phosphorylated MUC1-tail functions as a transcription factor that promotes expression of several genes such as survival genes and proliferation genes like β -catenin and p53 (Kufe, 2010). Figure 2.6 illustrates the binding of Gal3 to RTK and MUC1, activation of MUC1-tail phosphorylation, transport of the MUC1-tail by importin- β and change in gene expression.

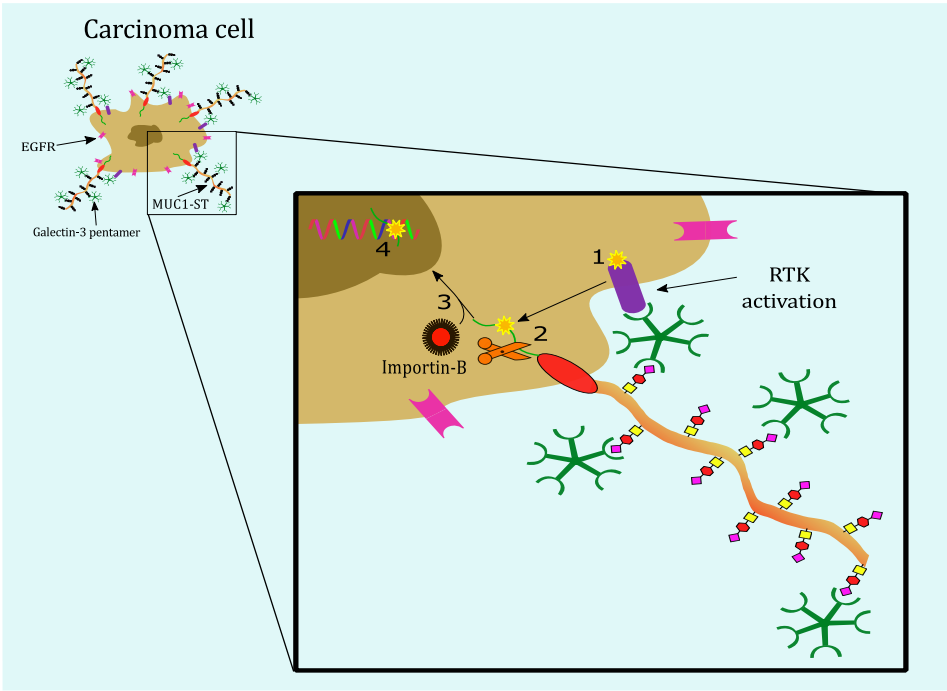


Figure 2.6: Activation of the intracellular tail of MUC1-C domain in carcinoma cells. (1) Binding of Gal3 to both MUC1 and RTK activates RTK. (2) Activated RTK phosphorylates the MUC1-tail which induce cleavage and oligomerization of the tail. (3) Importin- β transport the MUC1-tail to the nucleus where it (4) functions as a transcript factor.

2.4.2 Metastasis

One of several oncogenic outcomes of interaction between MUC1 and Gal3 is metastasis. Metastasis is a term used to designate cancer cells that spread through the blood vessel to secondary tumour sites. The large size of the MUC1-backbone allows it to function as a shield for smaller adhesion molecules such as E-selectin and CD44H found on the cell surface, even with the decrease in Core-2 O-glycans in cancer cells. This effect prevents the adhesion molecules on circulating cancer cells to interact with the blood vessel endothelium, and MUC1 has therefore been described as an anti-adhesion molecule [(Ligtenberg, Buijs, Vos, & Hilken, 1992), (Wesseling, Van Der Valk, & Hilken, 1996), (Kondo, Kohno, Yokoyama, & Hiwada, 1998)]. Interactions between MUC1(T) and Gal3 have been reported to re-distribute the MUC1-displacement on the cell surface, leading to an exposure of adhesion molecules that further interact with the endothelium. This allows the cancer cell to escape from the blood vessel and invade tissue [(Yu, 2007), (Xin et al., 2015)].

2.4.3 Downregulation of immuneresponse

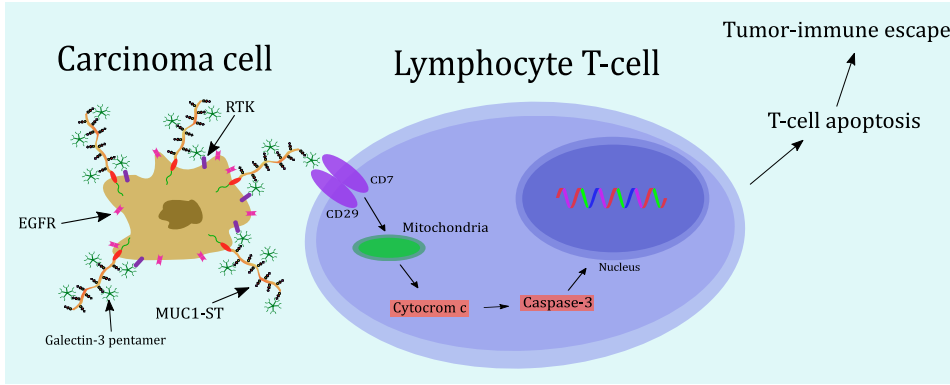


Figure 2.7: Illustration of MUC1-Gal3 induced lymphocyte T-cell apoptosis. Due to elevated levels and interactions between MUC1 and Gal3, the carcinoma cells are surrounded by a MUC1-Gal3 complex which prevent the lymphocyte T-cell to bind to cell surface substrates. Instead, the lymphocyte T-cell binds to Gal3 through its CD29 and CD7 receptors which induce secretion of Cytochrome-C from the mitochondria. Cytochrome-C activates Caspase-3 that in turn activates several death substrates, leading to an apoptosis signal of the T-cell and tumor-immune escape.

Cancer cells have several strategies in order to avoid the immune system. One of them is reported to be downregulation of immuneresponse by inducing lymphocyte T-cell apoptosis. The normal function of T-cells is to control normal activity of a cell by binding to different substrates on the cell surface (Kyewski, Suri-Payer, & SpringerLink, 2005). As explained, cancer cells have elevated levels of MUC1 expressed on the cell surface and an increased production of Gal3 (Kufe, 2010). The reported interaction between MUC1 and Gal3 (Yu et al., 2007) can lead to a formation of tightly packed MUC1-Gal3 complexes, surrounding the cancer cell. Further, when the MUC1-Gal3 complexes are surrounding the cell surface, the T-cell is not capable of binding to the substrates on the cell surface, but bind to Gal3 instead. Interaction between Gal3 and CD29 and CD7 simultaneously on T-cells have been found, and such interactions have been shown to lead to induced secretion of Cytochrome-C from the mitochondria out to the cytosol. Cytochrome-C activates Caspase-3 which further activates several death substrates. The death substrates are transported into the nucleus where they induce apoptosis of the T-cell, leading to an downregulation of immuneresponses to the cancer cell (Fukumori et al., 2003).

Chapter 3

Experimental theory

Several techniques can be used in order to quantify the interaction force between two molecules. Among these are the sensitive force probes atomic force microscopy (AFM) and optical tweezer (OT). Both instruments bring the molecules in contact, but differ in the manner of direct mechanical contact. OT use a laser beam to control the molecules, where AFM use a mechanical arm and a cantilever. In this master thesis OT has been used in order to obtain information about glycan-lectin interactions. The force curves obtained using OT have been further analysed to obtain information about interaction forces and energy landscape parameters. This chapter gives information of the basics for quantifying and analysing interaction forces.

3.1 Optical tweezers

OT is a sensitive optical instrument used in order to analyse binding forces between two molecules. In a dual trap OT, a laser beam which is split into two beams is used in order to trap the two particles at the same time. Of importance is the use of spherical polystyrene beads, characterised by a refractive index that is higher than this of water. This cause refraction of the laser light and thus transfer of momentum from photon ions in the laser light to the bead as further explained below. The sample solution is contained in a liquid cell which is sealed in order to prevent vaporisation.

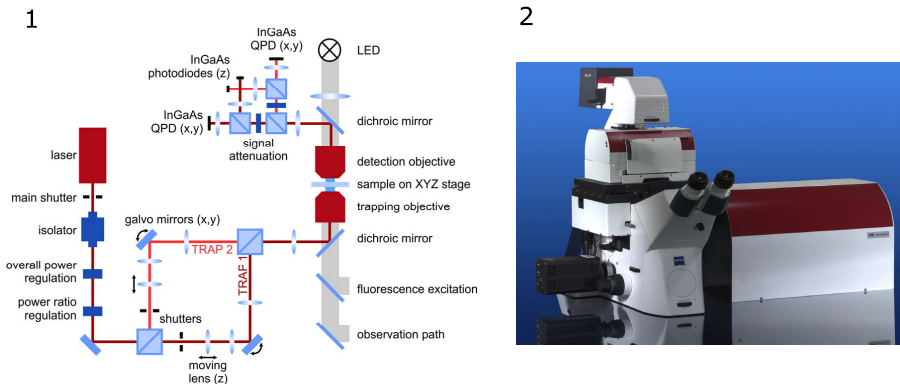


Figure 3.1: Illustration of OT instrument. Figure achieved from JPK Instruments.

Figure 3.1 shows the set-up and a photo of the OT instrument, present at the Department of Physics at NTNU. The figure is achieved from JPK Instruments and includes information about the position of the laser beam, the main shutter and the (dual) shutters, trap 1 and trap 2, high numeric aperture trapping and detection objective, the moving sample stage and the quadrant photo diode (QPD) detector. The instrument are also connected to a computer which allow the sample stage to be electronically managed, and a real-time camera that can be used to

observe the sample.

3.1.1 Optical trapping

A key element in OT is the laser beam with an Gaussian intensity profile as illustrated in figure 3.2. The Gaussian intensity profile tells how the photon intensity decrease from the centre of a laser beam to the edges. Further, equation 3.1 explains the decrease in photon intensity which increasing radius.

$$I_s = I_0 \exp\left(-\frac{2r^2}{\omega_0^2}\right) \quad (3.1)$$

The physical basis for trapping the polystyrene beads is the transfer of momentum from photons to the polystyrene beads. Newton defined of the momentum (p) of a particle proportionally to the velocity (v) to the particle ($p = m v$). For a photon, travelling at the speed of light, the velocity is at a so high level that the mass of the photon can be neglected $p = v$. The total energy can then be described as in equation 3.2.

$$E = p c \quad (3.2)$$

Where E is the total energy of a photon, p is the momentum of the photon and c is the speed of light in vacuum. Another equation of photon energy is given by equation 3.3.

$$E = \frac{h c}{\lambda} \quad (3.3)$$

Where λ refer to the photon wavelength and h is the Planck constant. By combining equation 3.2 and 3.3, the total momentum that is transferred from a single photon to the polystyrene beads by reflection or refraction is obtained (equation 3.4).

$$p = \frac{h}{\lambda} \quad (3.4)$$

Another important physical basis for the OT-instrument is presence of "*Rayleigh regime*" in the instrument. The "*Rayleigh regime*" appear when then wavelength (λ) to the photon are much smaller than the dimension (d) of the polystyrene bead: $\lambda \ll d$.

3.1.2 Axial and lateral trapping

As described, the transfer of momentum occur when the photons from the laser beam interact with the polystyrene bead. The transfer of momentum follows the Snell's law of refraction, described in equation 3.5 where the photons travel through

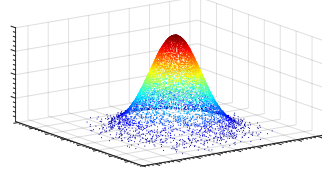


Figure 3.2: 3D-model of the Gaussian distribution of a laser beam, where the maximum photon intensity is in the centre of the beam and decreases to the edges.

the bead, resulting in a refraction that is dependent on the incident angel θ and change in refraction index n .

$$n_1 \sin \theta_1 = n_2 \sin \theta_2 \quad (3.5)$$

The OT-instrument is able to trap two beads in all three directions x, y and z by use of a shutter that split the laser beam into two separate beams, both with the same Gaussian distribution. The described transfer of momentum will result in two forces from the photon reflection and refraction that act on the bead, where the reflection result in scattering forces (F_1 and F_2) and the refraction result in gradient forces (G_1 and G_2). The scattering force act 90° on the refracted gradient force as illustrated in figure 3.3. Further, the same figure illustrate the axial and lateral trapping of the bead. The axial trapping in z-direction position the bead at the laser focus point due to equation 3.6 where the scattering and reflection forces equally affect the bead. As illustrated in figure 3.3:1, the bead are placed below the laser focus point resulting in $\sum F_{gradient} > \sum G_{scattering}$. This enforce the bead to retract towards the laser focus point where equation 3.6 is obtained.

$$\sum F_{gradient} = \sum G_{scattering} \quad (3.6)$$

Similar to axial trapping, lateral trapping is affected by the gradient force and scattering force. In figure 3.3:2, the bead is positioned in the laser focus point in z-direction which mean that equation 3.6 is obtained. The change in this figure is the gradient forces F_1 and F_2 that distribute unequally on the bead, due to the left shift in position from the centre of the laser beam. The left shift result in $F_1 < F_2$ which move the bead towards the right until $F_1 = F_2$ is obtained.

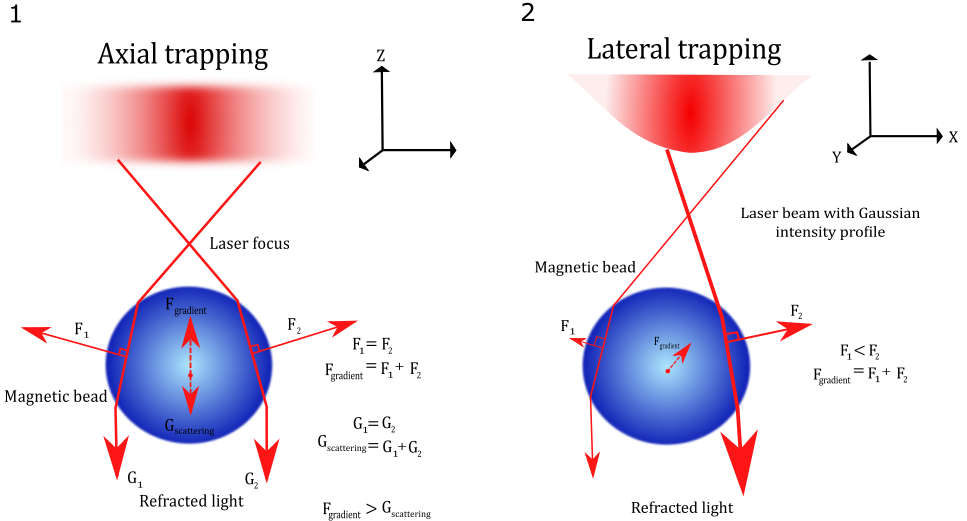


Figure 3.3: Illustration of axial and lateral trapping. (1) Axial trapping where the bead is positioned below the focus point, resulting in a movement of the bead towards the laser focus point. (2) Lateral trapping where the bead is positioned left in the beam, resulting in a right shift towards the centre of the beam.

3.1.3 Calibration

The OT-instrument use a quadrant photodiode(QPD)-detector in order to detect the signal achieved from the trapping of the bead. A photodiode is an device that converts light signal into an electrical signal. The trapping objective centre the laser beam where the refracted photons from the trapped bead are further spread in the detection objective. When the bead is trapped in the optical trap, it function as a small concave lens because it refract the photons that collide with it. On the back focal plane, positioned behind the detection objective, the refracted laser signal is detected by the QPD-detector. The back focal plane is the place where the light cross over one another, similar to the retina in a human eye. The QPD-detector have a circular shaped diode detector with four equally sized quadrants. The signal is received as a volt signal in the two lateral directions: x and y. This phenomenon is called back focal plane interferometry and is illustrated in figure 3.4. As illustrated in figure 3.4, a change in the beads position results in a photon amplitude shift that are presented on the back focal plane. The amplitude shift can be calculated by $f \sin \theta$. Furthermore, the sphere diameter (d) and a change in δ -signal, which represent the axial position of the bead, are detected by another photodiode as illustrated in the instrument overview in figure 3.1.

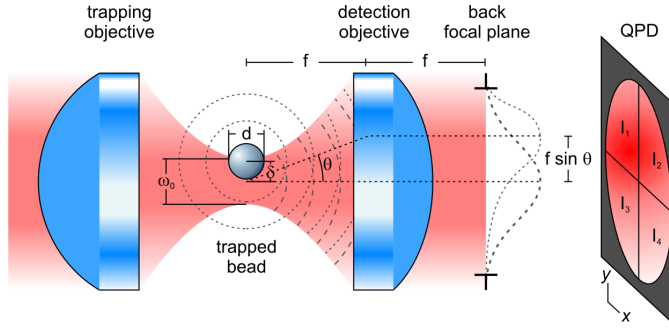


Figure 3.4: Illustration of the back focal plane interferometry phenomenon, where the refracted photons from the bead are detected on the back focal plane by a QPD-detector. The figure further illustrate how a change in the beads position, in this case in the edge of the beam, result in a photon amplitude shift that are presented on the back focal plane. The signal received by the QPD-detector is received as a volt signal in the two lateral directions: x and y. Figure achieved from JPK Instruments.

The displacement signal that the QPD-detector receive is calculated by equation 3.7 where the signal is calculated in both x and y-directions as Q_x and Q_y .

$$Q_x = (I_1 + I_3) - (I_2 + I_4) \quad Q_y = (I_1 + I_2) - (I_3 + I_4) \quad (3.7)$$

Brownian motion of a particle

The first person to describe Brownian motion was Robert Brown, that in 1827 reported observations of small pollen particles that appeared to randomly move around in a drop of water. This phenomenon was later verified to include all particles that was suspended in a fluid. Albert Einstein further published a paper in

1905 where he described the observations to be due to continuous collision of small particles from the surrounding media. Brownian motion was formally described as *"a stochastic process that models random continuous motion"* (Ibe, 2013, p.129-131). During calibration, information about the Brownian motions of each bead need to be obtained in order to eliminate the surrounding media's affect on each bead.

Spring constant

When the bead is trapped in the optical trap, the behaviour is similar to a spring with a certain mass attached to it, due to the forces that act on the bead explained in section 3.1.2 (Ding, Lai, Sakakibara, & Shinohara, 2000). The spring constant in the lateral directions in equation 3.8 can be determined by Hooke's law, where the force that act on the bead is correlated to the spring constant (k) and the displacement of the bead (x). The displacement of the bead and the use of Hooke's law is illustrated in figure 3.6.

$$F = -k x \quad (3.8)$$

The forces that act on the bead in axial direction are dependent in the spring konstant (k_z), the mass (m) of the particle and the viscous drag coefficient (D) and can be determined by equation 3.9 (Ding et al., 2000).

$$\frac{F}{m} = Z \frac{k_z}{m} + Z \frac{D}{m} + Z \quad (3.9)$$

The viscous drag coefficient that act on a spherical particle in low velocity speed can, according to Stokes Law, be determined by equation 3.10 where η is the viscosity to the surrounding media, and r is the radius of the particle (Ding et al., 2000).

$$D = 6 \pi \eta r \quad (3.10)$$

Lorentzian shape function

In order to calibrate the instrument it is crucial to include the Brownian motion, the trap stiffness, the drag coefficient and the Gaussian distribution. This is done by a Lorentzian shape function, presented in Eq. 3.11.

$$S(f) = \frac{k_B T}{\gamma \pi^2 (f_c^2 + f^2)} \quad \text{where } f_c = \frac{k}{2\pi\gamma}. \quad (3.11)$$

By use of the Lorentzian shape function presented in equation 3.11, the trap stiffness and the correlation between measured detector sensitivity and expected frequency are measured and calculated. As seen in figure 3.5, the correlation between measured detector sensitivity (V^2/Hz) and expected frequency (nm^2/Hz) yields a linear calibration curve within the linear range. The slope within the linear range is used in order to convert the volt-signal to force-signal. The calibration set-up is performed for all x, y and z directions.

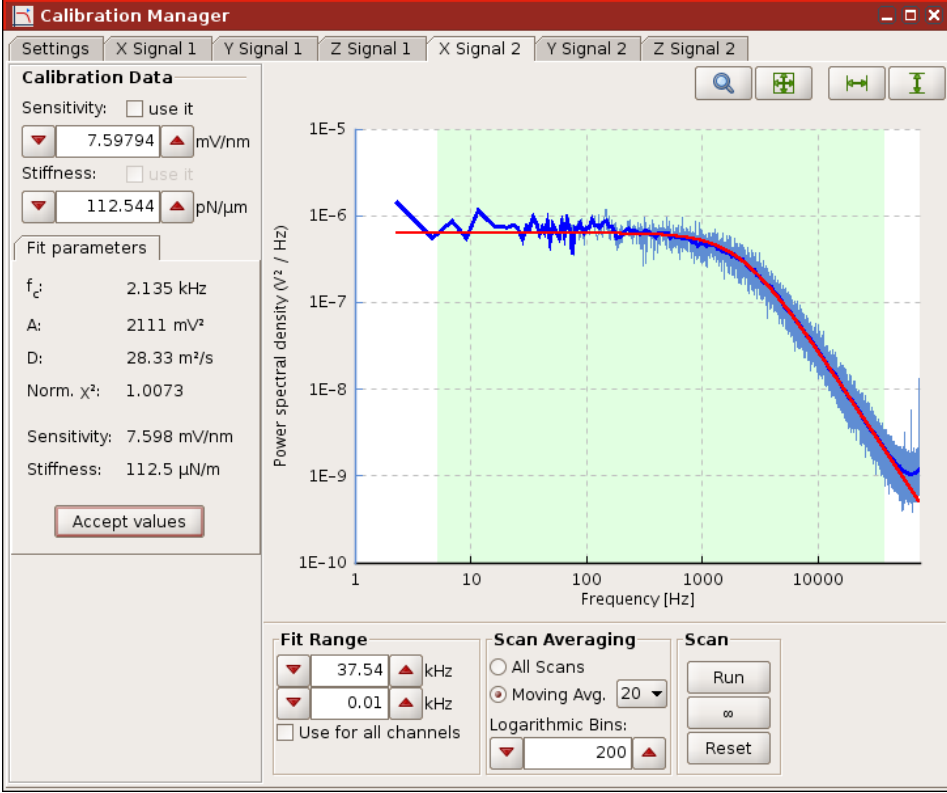


Figure 3.5: Screenshot of OT-calibration in NanoTracker software. The blue curve is obtained from the thermal noise that is derived from the observed particles movement inside the trap, and which is due to e.g. Brownian motions. The red curve is obtained from the fitting of the Lorentzian curve function (equation 3.11). From the red curve, information about sensitivity and stiffness is derived. Figure achieved from JPK Instruments.

3.1.4 Determination of intermolecular interaction forces using OT

The sensitivity constant (β) and the the spring constant (k), derived from the calibration, are used in order to translate the interaction force from intensity signal (Q) to pN force. The intensity signal derived from the QPD-detector is multiplied with the sensitivity constant in order to translate the change in intensity signal to the change in position (x). Further, the spring constant is multiplied with the the change in position in order to calculate the pN force that drag the the bead out of stable position. Figure 3.6 illustrate the coherence between the change in the position of the bead and the yield in pN force. In order to calculate the total interaction force in the dual beam system, all the forces that act on the two beads are added together.

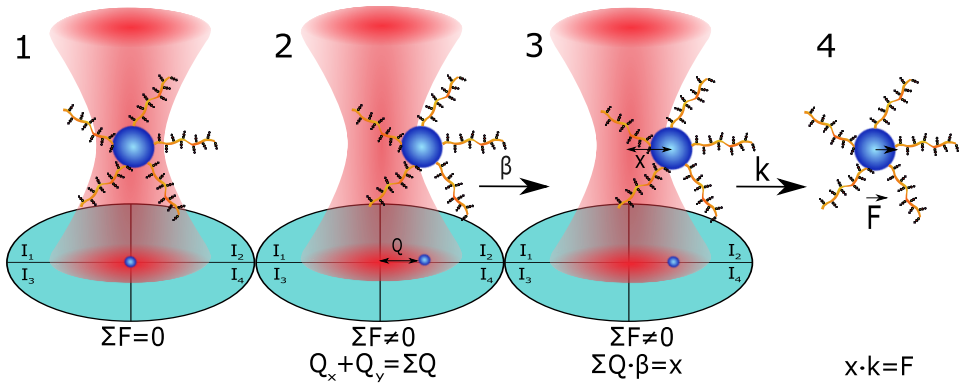


Figure 3.6: Illustration of calculation steps in OT in order to translate the interaction force from intensity signal to pN force. (1) The calibration is performed where no external forces act on the bead. The β -constant (sensitivity) and the k -constant (trapstiffness) are derived from the calibration. (2) When interaction occur, the change in the intensity signal (Q) is translated to the change in position (x) (3) by multiplying it with the β -constant. Furthermore, the complete signal translation (4) occur when the k -constant is multiplied with the observed change in bead position. The $\Sigma F \neq 0$ indicate that external forces are acting on the bead.

3.2 Dynamic force spectrum

The main aim with analysing the rupture events between two interacting proteins is to obtain information about the strength of the interaction. The intermolecular forces that bind the proteins together are mainly from non-covalent interactions such as van der Waals forces, hydrogen bonds and hydrophobic forces. Non-covalent interactions are characterised by an inherent limited lifetime and will rupture if a force pull the molecules apart for a sufficient strength and time (Evans, 1999). In order to obtain information about properties of the intermolecular bond such as e.g. lifetime and most probably rupture force between the two molecules, a dynamic force spectrum is often used. This section will give a brief introduction to the theorems behind the dynamic force spectrum (DFS) and its applications.

3.2.1 Free energy landscape and the two state model

During interaction between the molecules, they form several conformation states that have specific characteristics. Each state is connected together by free energy parts, that together form a free energy landscape. The free energy landscape of a protein or other biological complexes is dependent on e.g. ability to rotate, different electronic states and the protein configuration of side chains and folding. In order to enter a bound state, the molecules have to receive/absorb a certain amount of energy called activation energy. The level of activation energy needed differ from molecules to molecules. Additionally, a molecular pair will often, due to the composition of the molecules, have several activation energy barriers to overcome during dissociation. This gives rise to the two state model, which is a simplified model where the different energy barriers during dissociation are illustrated as

two main barriers. A simulation of how the free energy landscape is organised including a graphical illustration of the two state model, is presented in figure 3.7.

Further, the realistic energy landscape include a variation in depth for the wells and peaks for the different dissociation energy barriers. The reaction rate between molecule A and B ($k_{A \rightarrow B}$) can be described in equation 3.12, where the well and peak width are defined as l_A and l_t and the dissociation energy as ΔG_{tA} . Further, ζ defines the frictional coefficient.

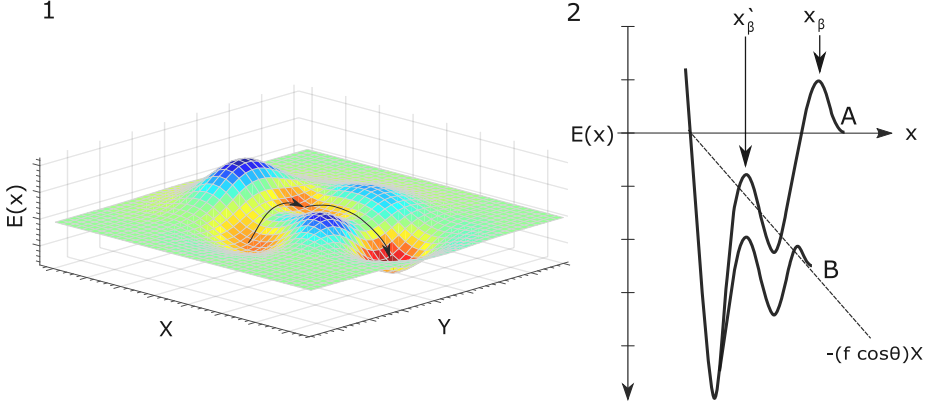


Figure 3.7: A simulation of how the free energy landscape is organized including a graphical illustration of the two state model. (1) The free energy landscape is illustrated in a 3D model with the energy-level on the z-axis and the distance (x) on the x- and y-axis. (2) A graphical illustration of the two state model, reproduced from (Evans & Ritchie, 1997), with the energy-level on the y-axis and the distance (x) on the x-axis. x_β denotes the inner energy barrier with the lowest energy state, where the x'_β denotes the outer energy barrier. The shift with the factor $-(f \cos \theta)x$ from graph A to graph B are due to the mechanical forces that are added during dissociation in the analysis, and illustrated with a dotted line. In praxis, the shift results in the inner barrier becoming the determinant of the rupture force instead of the outer barrier.

$$k_{A \rightarrow B} = \frac{k_B T}{\zeta l_t l_A} e^{-\frac{\Delta G_{tA}}{k_B T}} \quad (3.12)$$

During analysis, the dissociation energy needed to rupture the interaction has to be mechanically added by forcing the molecules to dissociate. Furthermore, the applied mechanical force of dissociation energy have been proven to be strongly important for the magnitude of the energy barriers in the landscape (Evans & Ritchie, 1997). In figure 3.7, the graphical illustration of the two state model also include a shift from graph A to graph B. This illustrate the distribution of the applied mechanical force on the energy landscape by the factor $-(f \cos \theta)x$, where f denotes the rupture force. From these findings, the force loading rate has been applied and defined as the external force that has been applied per time unit (df/dt).

The loading rate is indeed an important parameter to include in order to gain information about the energy landscape of the molecules. From these findings a

DFS-plot can be created based on the information about loading rate and rupture force for a large dataset of interactions. Figure 3.8 illustrates an example of a DFS-plot where log loading rate on the x-axis is plotted against rupture force on the y-axis. The plot further shows a shift in the slope, which is due to the applied mechanically force that corves the molecules to dissociate following an alternative pathway in the energy landscape.

3.2.2 Calculations

A chemical reaction between two molecules with equal affinity for each other can be described as in equation 3.13, where the concentration of $[AB]$ -complex is dependent on the association rate (k_{on}) and the dissociation rate (k_{off}) to the two molecules (Bizzarri & Cannistraro, 2010).

$$\frac{d[AB]}{dt} = k_{\text{on}}[A][B] - k_{\text{off}}[AB] \quad (3.13)$$

The dissociation rate is further inverse proportional with the lifetime (τ) of the $[AB]$ -complex as denoted in equation 3.14.

$$\tau = \frac{1}{k_{\text{off}}} \quad (3.14)$$

Observations have revealed k_{off} to be influenced by the external force, which further can be described in equation 3.15 where k_B denotes the Boltzmann constant and T denotes the temperature. The F factor denotes the rupture force and the x_β factor denotes the distance from the rupture force determine energy barrier to the binding well, as illustrated in figure 3.7 (Bizzarri & Cannistraro, 2010).

$$k_{\text{off}}(F) = k_{\text{off}} \exp\left(\frac{F x_\beta}{k_B T}\right) \quad (3.15)$$

In order to determine the overall most probable unbinding force (f^*) at a given loading rate for the molecules, the DFS-plot is divided into subgroups on the basis of the loading rate and further plotted in a Bell-Evans histogram plot. The Bell-Evans plot is a histogram where the rupture force is plotted against the number of observations (Evans & Ritchie, 1997). Equation 3.16 is further fitted to each histogram which describe the most probability distribution of the most likely rupture force at the given loading rate (Dudko, Hummer, & Szabo, 2008). Figure 3.10 illustrates the relationship between the DFS-plot, a 3D-model of the DFS-plot and the Bell-Evans subgroups. From each subgroup, a f^* value is determined from the peak ($f''(x) = 0$) of each histogram. From the most probable rupture force, from peak determination, the corresponding loading rate (r_f) is denoted.

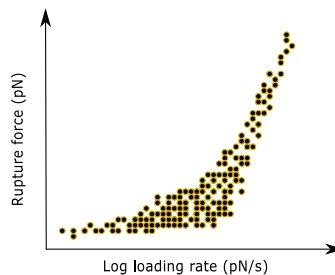


Figure 3.8: Illustration of a DFS-plot for interaction forces between two molecules, where the log loading rate on the x-axis are plotted against rupture force on the y-axis. The figure show a shift in the slope where the shift is due to the change from the outer to the inner energy barrier in the free energy landscape.

$$P(f) = \frac{\exp\left(-\int_0^F [r_f(f)\tau(f)]^{-1} df\right)}{r_f(F)\tau(F)} \quad (3.16)$$

In equation 3.16, r_f denotes the force loading rate, $P(f)$ denotes the probability distribution of the most likely rupture force at the given loading rate and τ denotes the lifetime. The f^* value and the corresponding $\ln(r_f)$ value for each subdistribution have proportional coherence in a DFS-plot by equation 3.17 (Sulchek, Friddle, & Noy, 2006).

$$f^* = \frac{k_B T}{x_\beta} \ln\left(\frac{r_f x_\beta}{k_{\text{off}} k_B T}\right) \quad (3.17)$$

The k_B constant denotes the Boltzmann constant and T denotes the absolute temperature. In each subgroup, equation 3.16 is used to find the f^* value and further equation 3.14 and equation 3.15 to find the k_{off} and the x_β . Another method to find the k_{off} and the x_β is to use the f^* and the corresponding r_f value from each subgroup and create a DFS-plot on that basis. Figure 3.9 illustrates a simplification of the DFS-plot in figure 3.8, where the two energy barriers have resulted in a change in the linear slope value. Each slope can be calculated from equation 3.18 and is due to the shift from the outer to the inner energy barrier, being the rate-determinant for the reaction as illustrated and explained in figure 3.7.

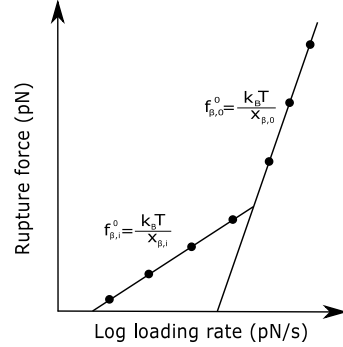


Figure 3.9: Simplified illustration of a DFS-plot for interaction forces between two molecules, where the f^* value are on the y-axis and the corresponding $\ln(r_f)$ value for each subdistribution are on the x-axis. The figure further illustrate the shift in slope for the DFS-plot, which is due to the change in supply of external force.

$$\Delta f_\beta = f_{\beta,0}^0 - f_{\beta,i}^0 \quad \text{where } f_{\beta,0}^0 = \frac{k_B T}{x_{\beta,0}} \text{ and } f_{\beta,i}^0 = \frac{k_B T}{x_{\beta,i}} \quad (3.18)$$

The k_B constant denotes the Boltzmann constant, T denotes the absolute temperature and f_β denotes the slope of the curve. From equation 3.17, the k_{off} value can for each linear regime be calculated based on the intercept where $r_f = 0$. The x_β factor can be further determined (equation 3.18).

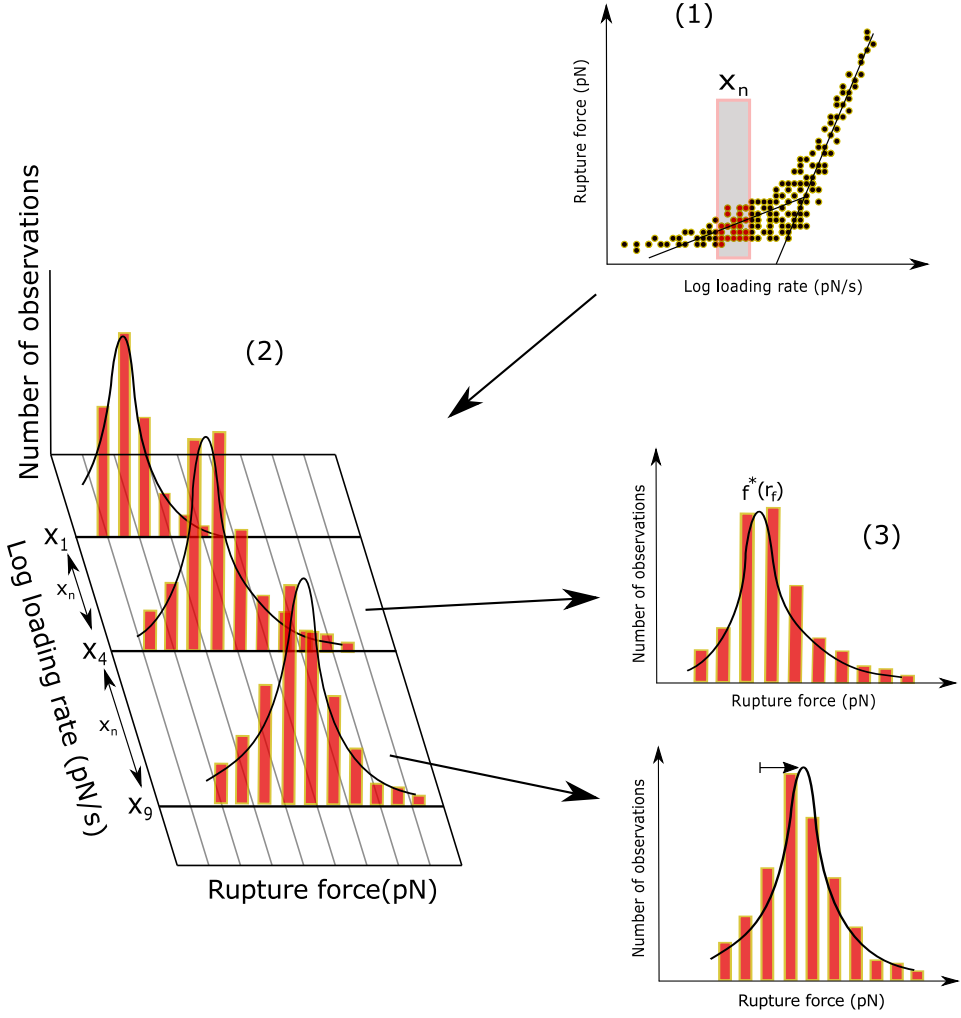


Figure 3.10: 3D-illustration of the DFS-plot and the relationship between the DFS-plot and the Bell-Evans subgroups. (1) A graphical illustration of the DFS-plot similar to Fig.3.8, where the shaded area illustrate how the interactions are divided into subgroups (x_n) on the basis of the loading rate values. (2) The same DFS-plot is illustrated as a 3D-model where also the information about the number of observations are included on the z-axis. Each subgroup is from the 3D-model illustrated as a Bell-Evans plot (3) where the peak and loading rate to the corresponding peak value of each histogram is determined. Due to the linear correlation between F^* and r_f , the different subgroups have a shift in peak/loading rate value, as illustrated with the black arrow in the histogram down to the right.

3.3 Finding the rupture force and loading rate

In order to find the f^* , k_{off} and x_β values described in the previous section, the rupture force and loading rate from each observed rupture events need to be conducted. The JPK OT-instrument generates a text-file with a huge amount of information about the rupture event including the calibration parameters. The text-file can further be used in a IDL-based analysis program, created by Bjørn Stokke at the Department of Physics at NTNU. The program has two main process, called pre-process and post-process, where the detected change in force in x, y and z-direction for both beads are combined and further analysed. This section gives a brief explanation of the theory about how the rupture force and loading rate for each rupture event are conducted.

3.3.1 iNanoTrackerOT3DPreProcess software

iNanoTrackerOT3DPreProcess program use the information from the text-file to create several graphs for both beads in x, y and z-directions. Each graph contains information about one of the beads in one of the three directions. The created graphs use the information about bead displacement (nm) on the x-axis and the interaction force (nN) on the y-axis. In order to combine all graphs to one single graph, the two curves in every graphs need to be combined. This is done by calculate the change in interaction forces for the retract curve and the approach curve, shown in equation 3.19 where ΔF refer to the change in curves.

$$\Delta F = \text{Retract} - \text{Approach} \quad (3.19)$$

The result from equation 3.19 is, when no interaction is observed, a straight line. Each curve is then plotted in a new "force vs distance" plot and further combined to a single curve as shown in equation 3.20.

$$\sum F_1 = \Delta F x_1 + \Delta F y_1 + \Delta F z_1 \quad \sum F_2 = \Delta F x_2 + \Delta F y_2 + \Delta F z_2 \quad (3.20)$$

Figure 3.11 show a print screen image of the interaction analysing in the iNanoTrackerOT3DPreProcess program. The graphs at the bottom show the retract and approach curves to both beads in x, y and z-directions, with the change in retract-approach graphs illustrated in a "force vs distance" plot to the right in the picture. By further adding $\sum F_1$ and $\sum F_2$ together, the combined curve, is obtained (figure 3.11:3).

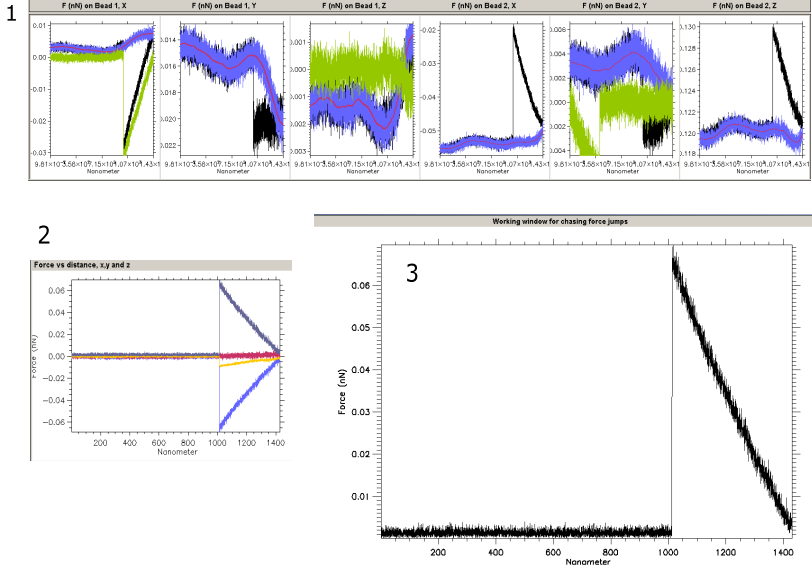


Figure 3.11: Print screen of interaction analysis in iNanoTrackerOT3DPreProcess program. (1) The graphs show the change in forces for both bead 1 and 2 in all three dimensions, x, y and z. The black and purple curves correspond to the approach and retract curves. The red curve represent the mean value for the purple curve, where the green curve represent the difference between the retract and approach curves (ΔF). Further, the baseline in the green ΔF -curve is reset to zero force. (2) The data conducted from the previous part are plotted together in one "Force vs distance" plot. The positive force-values are conducted from bead 1 and the negative force-values from bead 2. (3) By combining all curves from bead 1 and 2, the black curve is conducted where the plot represent the interaction force at a specific loading rate.

3.3.2 iNanoTrackerOT3DPostProcess software

The text-file with the results from the analysis in the iNanoTrackerOT3DPreProcess program gives the basis for analysis in the iNanoTrackerOT3DPostProcess program. The program uses the combined curve shown in figure 3.11 to calculate the rupture force and the loading rate. The loading rate is defined as the external force that is being applied per time unit (df/dt) and is calculated from the slope as shown in equation 3.21, where f denotes the force and d denotes the distance.

$$r_f = \frac{\Delta y}{\Delta x} = \frac{\Delta f}{\Delta d} \quad (3.21)$$

Of importance is the difference between the two f values and the d values, due to the exponential behaviour of the correlation between force and displacement. Further, the rupture force is calculated from the maximum force value in the curve, where the maximum value is compared with the baseline value. An interaction curve can have several rupture events due to multiple interactions. Figure 3.12 show a print screen image of interaction analysis in the iNanoTrackerOT3DPostProcess program, where the loading rate and rupture force are found.

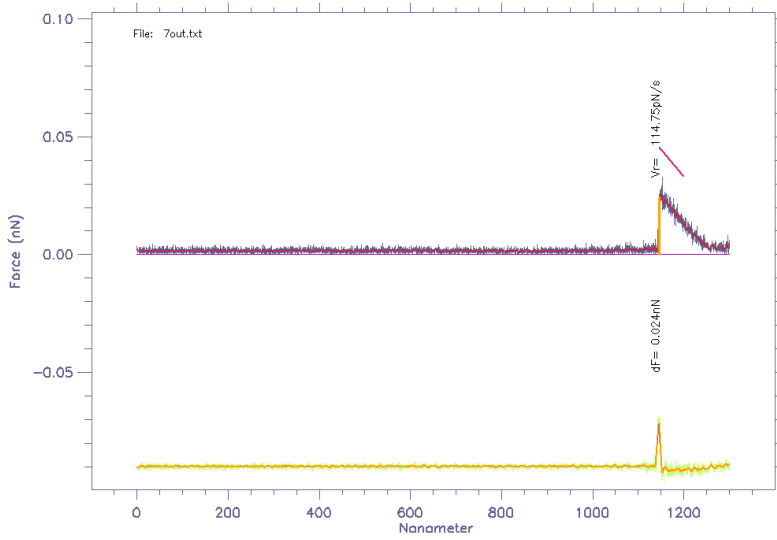


Figure 3.12: Print screen of interaction analysis in the iNanoTrackerOT3DPostProcess program. The purple curve show the completely combined curve from iNanoTrackerOT3DPreProcess, where the red curve is the result of a smoothing operation performed on the data underlying the purple curve. The loading rate is obtained from a linearisation of the last pixels of the red curve prior to the rupture event. The green curve show the second derivative of the purple curve, where the rupture force is conducted from the peak in the curve.

Chapter 4

Experimental Setup

The experiments were carried out by use of an optical tweezer dual beam set-up, where two polystyrene beads are brought into contact. The force jumps reflecting the forced rupture of intermolecular bonds observed during the retraction of the beads, were further analysed in the iNanoTrackerOT3D software. The interaction abilities of MUC1(ST), MUC1(T), MUC1(Tn) and MUC1(Na) with Gal3 were investigated. Additionally, interactions in negative controls such as Gal3, MUC1(ST) and MUC1(T) in contact with blank polystyrene bead, immobilized using the same protocol as for the other samples but without protein, were investigated.

The MUC1 samples were produced using wild type and mutant CHO cell expression systems as described in [(Beatson et al., 2015), (Link et al., 2004)]. The molecules contained the extracellular part of human MUC1, including 16 MUC1 TR-regions. The molar mass of the core polypeptide chain of the MUC1 molecules was 46 kDa. They also carried an IgG domain with molecular weight of about 50 kDa. Each tandem repeat had 5 glycosylation sites. Gal3 was obtained from R&D Systems Inc. Minneapolis, USA.

4.1 Protein immobilization

In order to immobilize the proteins onto polystyrene beads, 120 μL boric acid and 2.0 $\mu\text{g}/\mu\text{L}$ EDC(1-Ethyl-3-(3-dimethylaminopropyl)carbodiimide) was mixed in an eppendorf tube. The EDC-molecule is used in order to crosslink a carboxylic presenting molecule with an amine presenting molecule. Due to the limited stability of Gal3 and the possibility of degradation, all reagents and samples were incubated and stored on ice at all time. 50 μL of the EDC/boric acid mixture was then added to two other eppendorf tubes. Further, to one of the tubes was added 0.01 $\mu\text{g}/\mu\text{L}$ Gal3 and 2.0 μL 3.07 μm sized acid-functionalised polystyrene beads. To the other tube was added 0.1 $\mu\text{g}/\mu\text{L}$ MUC1-protein with different glucose structure and 1.0 μL 2.10 μm sized amino-functionalised polystyrene beads. Both samples were carefully mixed and incubated on ice for one hour. After the incubation, both tubes were centrifuged for 60 s at 6000 rpm. The supernatant was then removed and 200 μL of 100 mM HEPES (4-(2-hydroxyethyl)-1-piperazineethanesulfonic acid) buffer at pH 6.9, containing 1 mM CaCl_2 and 1 mM MnCl_2 , was added. After careful mixing using a pipette, the tubes were again centrifuged with the same speed and duration. The same steps with removal of supernatant, addition of 200 μL Hepes buffer and centrifugation were repeated one time. After the 3rd removal of the supernatant, 200 μL Hepes buffer was added to the MUC1-sample and 100 μL Hepes buffer was added to the Gal3-sample.

4.1.1 PLL-PEG coating protocol

PLL-PEG(PLL(20)-g[3.5]-PEG(2)) coating was used in order to create a non-polar coating on the glass surface, which prevent the beads from being permanently stuck on the glass surface. Each circular glass slide was placed in a circular plastic petri dish, and 1000 μL PLL-PEG working solution was added. After 1 hour incubation in room temperature, the PLL-PEG solution was removed and transferred back to

a tube that was stored in the fridge. The reason for this was PLL-PEG can be reused several times to coat the glass surface. 1000 μL of 1 mg/mL bovine serum albumin (BSA) reagent was then added to the glass slide and removed. 1000 μL milli-Q water was then added to the plate and removed. Each glass slide was then placed on some fine paper, approximately vertical to the paper with the pipettbox used as a wall, and allowed to air-dry for approximately 30 minutes. Of importance is the fact that the PLL-PEG coating can be damaged during mechanical contact.

4.2 Quantification of intermolecular interactions

The quantification of the intermolecular interactions was performed by use of the JPK NanoTracker instrument as illustrated in figure 3.1.

4.2.1 Preparation of the liquid cell

A liquid cell is a sample housing that can be filled with a liquid and sealed. By this, vapourisation of the sample can be prevented which inhibit liquid flow in the cell. The housing is build up by a circular cover glass which is coated with PLL-PEG, two stripes with double-sided tape and a rectangular cover glass on the top. Figure 4.1 presents an illustration of a liquid cell used in the OT-instrument. In order to add a sample containing both protein samples, 20 μL from both sample tubes are mixed together in a third tube. The precise volume needed to fill up the liquid cell depends on the volume inside the liquid cell. For the liquid cells used in this study, approximately 15 μL from the combined samples in the third tube was added on the edges to the liquid cell. In order to seal the liquid cell, nail polish was added between the tape stripes and the rectangular cover glass as illustrated in figure 4.1.

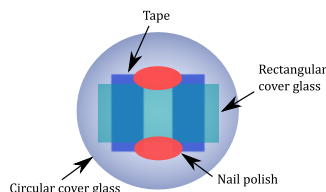


Figure 4.1: Illustration of a liquid cell used in the OT-instrument. The cell consists of a circular cover glass, two stripes with double-sided tape, a rectangular cover glass and nail polish for sealing.

4.2.2 Optical settings and calibration

Optimisation of the relative position of the lenses with respect to the samples was obtained through use of the Köhler illumination protocol. The Köhler illumination protocol was performed by closing the field diaphragm of the instrument and subsequent imaging of the field diaphragm by use of the trapping objective. The light intensity was then adjusted to the edges of the circular light source become clear. The field diaphragm was then opened and the calibration protocol could be performed.

The calibration was performed for each of the two beads of different sizes (2.01 μm and 3.07 μm) trapped in separate traps. The calibration was performed by

use of the automated procedure implemented in the software. After pressing the "run"-button, the brownian motion of each of the beads was determined and the spring constant was determined based on 5 parallel measurements, as explained in chapter 3. The position of the signal on the QPD-detector was set to zero for each trap by use of the "offset correction" under the "signal"-tab.

4.2.3 Parameter settings and analysing

During measurements, the beads were placed with an initial separation distance of about 1.0-1.5 μm . One of the beads were kept stationary and the other moved with a constant speed of 0.5 $\mu\text{m/s}$. The beads were gradually brought in contact by adjusting their separation distance by 0.01-0.002 μm between each run. A delay time of 0-0.5 s was sometimes included if no interactions was observed.

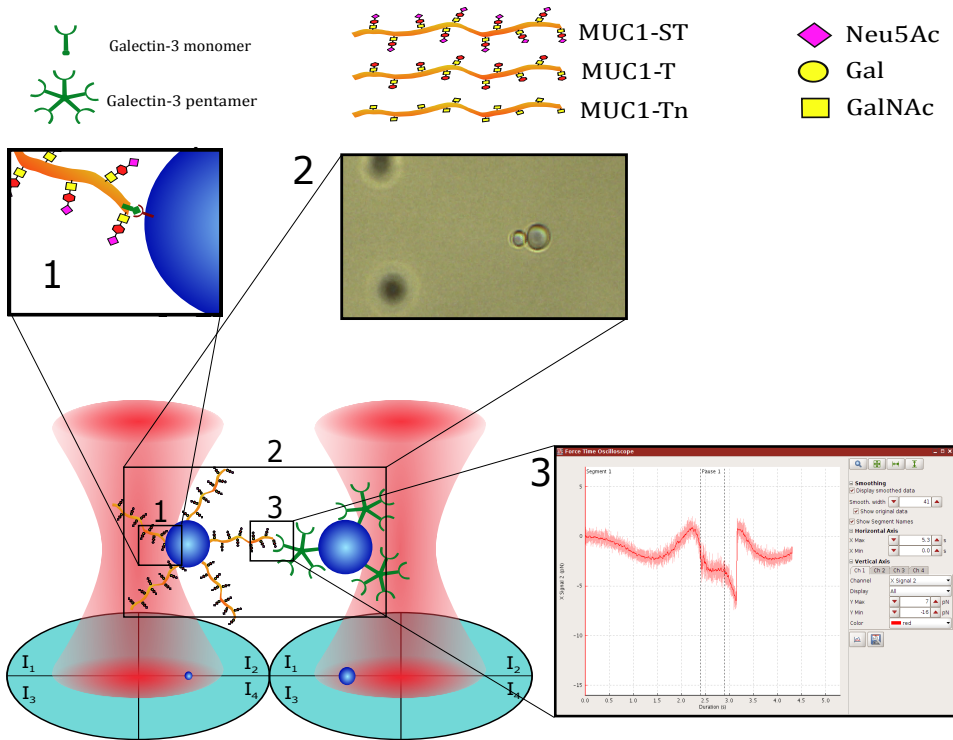


Figure 4.2: Overview of the important steps performed in order to analyse interaction between MUC1 and Gal3 in OT. (1) The proteins are covalently anchored to the polystyrene beads. (2) The different sizes on the beads are of importance in order to discriminate between the different proteins that are brought in contact. (3) The interaction force can further be observed as a distinct drop in the curve, due to the position changes in the optical trap. A graphical explanation of the Gal3 monomer and pentamer formation, the MUC1 formation and the sugar-residues that yield the ST, T and Tn antigens on MUC1, is added on the top of the overview illustration.

Figure 4.2 shows an overview of the important steps included in the experimental procedure in order to analyse the interactions between MUC1 and Gal3 using

OT. The proteins, covalently anchored to the beads by use of the EDC-molecule, were brought in contact by moving one of the optical traps. The beads are of different sizes in order to discriminate between the different molecules attached on the beads. Further, the rupture of the interaction that spontaneously forms between the MUC1 and Gal3 proteins resulted in a distinct drop in the curve, due to the position change in the optical trap.

4.3 Data processing

The data processing in the iNanoTrackerOT3D software was performed as described in chapter 3. The DFS-analysis described in the same chapter was created and analysed in the ForceSpecAnalyse-software in IDL.

Chapter 5

Results

Interactions between the glyco-protein MUC1 and the lectin Gal3 were investigated by use of the OT-instrument. Investigations of MUC1 and Gal3 showed Gal3 to interact with MUC1(T) and MUC1(ST). Further, Gal3 does not or only to a low extent interact with MUC1(Tn) and MUC1(Na). This chapter presents the experimental data collected as part of this master thesis, and which formed the basis for the conclusions drawn.

5.1 MUC1(T) interacts with Gal3

The data were obtained by coating polystyrene beads with MUC1(T) and Gal3. The procedure for protein immobilization presented in section 4.1 was followed. Investigation of MUC1(T) and Gal3 show some typical interaction as shown in figure 5.1a. The figure present a number of curves in order to view some examples of the observed interactions. The histogram presentation in figure 5.1b shows a combined histogram for all 456 interactions. The peak in the histogram is approximately 20-37 pN with no interactions above 80 pN. When increasing the density of molecules immobilised onto the interacting surfaces, the peak in the histogram was observed to shift to the right (data not shown).

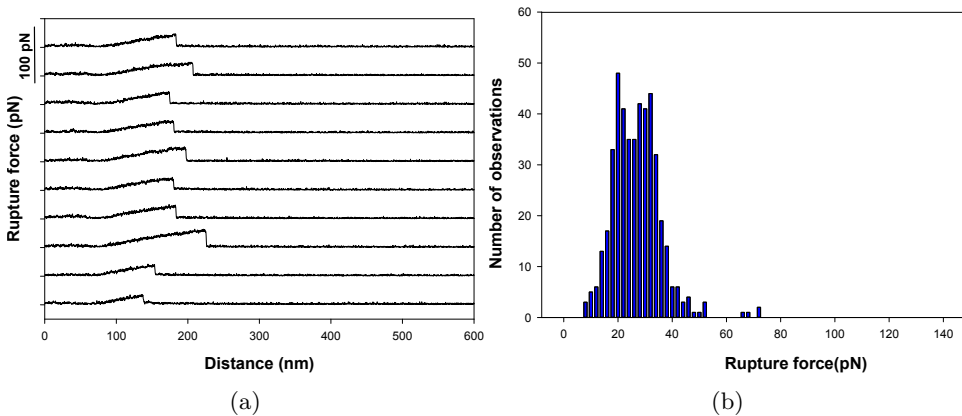


Figure 5.1: Gallery and histogram presentation of MUC1(T)-Gal3 interactions. **(a)** Examples of typical force versus inter-bead distance curves obtained for MUC1(T) – Gal3 interactions. The curves were obtained when using the experimental conditions explained in chapter 4. For each observed rupture event, the loading rate r_f was determined based on the slope of the force curve prior to bond rupture, while the height of the jump reflects the magnitude of the unbinding force f . **(b)** Distributions of the strength of the intermolecular rupture events observed between MUC1(T) and Gal3 obtained in optical tweezer experiments using polystyrene beads functionalized with MUC1(T) and Gal3. For this molecular system, 456 forced rupture events were collected and included in the analysis.

5.2 MUC1(ST) interacts with Gal3

The data was obtained by coating polystyrene beads with MUC1(ST) and Gal3. Investigation of MUC1(T) and Gal3 show some typical interaction as shown in figure 5.2a. The figure presents a number of curves in order to view some examples of the observed interactions. The histogram presentation in figure 5.2b show a combined histogram for all 1618 interactions. The peak from the histogram is approximately 30-40pN with interactions up to 140pN observed. When increasing the density of molecules immobilised onto the interacting surfaces, the peak in the histogram was observed to shift to the right (data not shown).

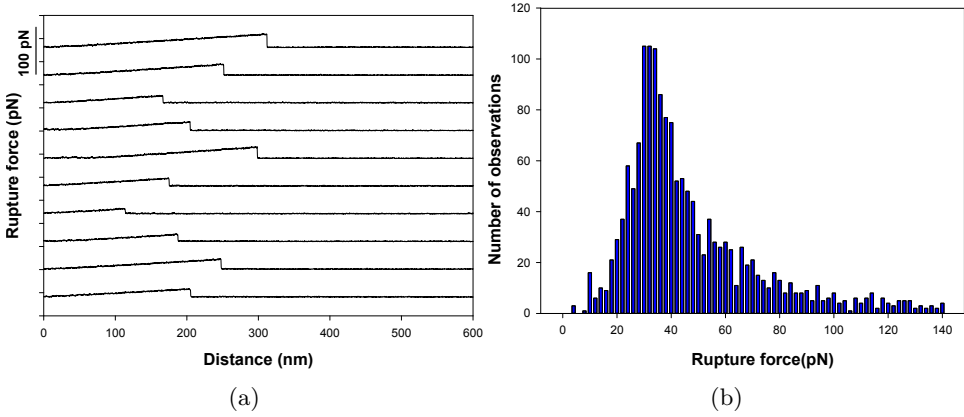


Figure 5.2: Gallery and histogram presentation of MUC1(ST)-Gal3 interactions. **(a)** Examples of typical force versus inter-bead distance curves obtained for MUC1(ST) – Gal3 interactions. The curves were obtained when using the experimental conditions explained in chapter 4. For each observed rupture event, the loading rate (r_f) was determined based on the slope of the force curve prior to bond rupture, while the height of the jump reflects the magnitude of the unbinding force f . **(b)** Distributions of the strength of the intermolecular rupture events observed between MUC1(ST) and Gal3 obtained in OT experiments using polystyrene beads functionalised with MUC1(ST) and Gal3. For this molecular system, 1618 forced rupture events were collected and included in the analysis.

5.3 MUC1(Tn) and MUC1(Na) do not interact with Gal3

The results from attempts to observe interactions between MUC1(Tn) and Gal3 or MUC1(Na) and Gal3 are presented in figure 5.3. Both antigen-structures do not show interaction between the MUC1 and Gal3 coated polystyrene beads. The data was obtained at the same conditions as for the MUC1(T) and MUC1(ST) samples.

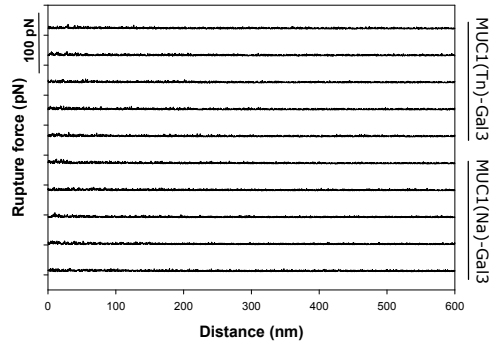


Figure 5.3: Gallery presentation from some interaction-curves between the complex MUC1(Tn)-Gal3 and MUC1(Na)-Gal3. The displacement distance on the x-axis is plotted against the rupture force on the y-axis.

5.4 Rupture frequency

As described by (Celik & Moy, 2012), unspecific glycan-lectin interactions can occur. In order to distinguish between unspecific interactions and real interactions, the rupture frequency [$P_{int}(\%)$] were determined for some chosen datasets. The force by which the two beads are pushed together can vary between different samples. In order to have as equally conditions as possible, the number of interactions that occur after an observed interaction event was observed were counted for a serie of 20 subsequent force versus distance curves. The rupture frequency is further determined based on the inspection of at least two independent samples of functionalised beads. For each sample, 5 independent pairs of beads were investigated. The rupture frequency analysis is presented in table 5.1, where the MUC1(ST) and MUC1(T) show a 42.8 % and 32.0 % rupture frequency, respectively with a standard deviation(SD) of 26 and 16. The MUC1(Tn) and MUC1(Na) show 0.5 % rupture frequency with a SD of 2 and 1. The negative controls of blank polystyrene beads against Gal3, MUC1(ST) or MUC1(T) gave 3.5 %, 0.0% and 7.8 % rupture frequency with a SD of 6, 0 and 7. Figure 5.4 presents graphical presentation of the data presented in table 5.1.

Table 5.1: The overall rupture frequency [$P_{int}(\%)$] are carried out from the interaction between Gal3 and the MUC1-attached ST, T, Tn and Na antigens. Information about interactions between blank polystyrene beads and Gal3, MUC1(ST) or MUC1(Tn) were used as negative control. The rupture frequency is determined based on bead couples where three negative samples were 3.07 μm COOH-functionalised bead with either Gal3 or no protein (blank), and the other 2.01 μm bead was NH₂-functionalised with either a mucin or no protein (blank). For simplicity, MUC1(ST)-Gal3 bead couples are in the figure abbreviated ST, MUC1(T)-Gal3 are abbreviated T, MUC1(Tn)-Gal3 are abbreviated Tn and MUC1(Na)-Gal3 are abbreviated Na. The standard deviation (SD) were further calculated from the rupture frequency of each analysis.

Rupture frequency		
Antigen	$P_{int}(\%)$	SD
ST	42.8	26
T	32.0	16
Tn	0.5	2
Na	0.5	1
Blank - G3	3.5	6
Blank - ST	0.0	0
Blank - Tn	7.8	7

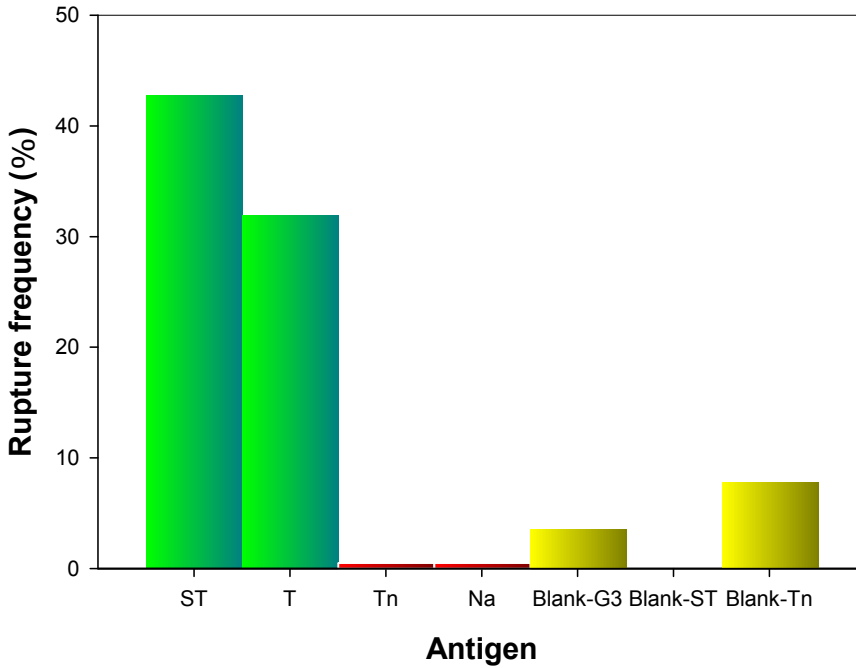


Figure 5.4: An graphical presentation of the rupture frequency data presented in table 5.1. The rupture frequency is determined based on bead couples where three negative samples were 3.07 μm COOH-functionalised bead with either Gal3 or no protein, and the other 2.01 μm bead was NH₂-functionalised with either a mucin or no protein (blank). For simplicity, MUC1(ST)-Gal3 bead couples are in the figure abbreviated ST, MUC1(T)-Gal3 are abbreviated T, MUC1(Tn)-Gal3 are abbreviated Tn and MUC1(Na)-Gal3 are abbreviated Na.

5.5 Non-exponentially increasing loading rate

As described in chapter 3, the loading rate is expected to increase until the rupture event is observed. The force versus distance curves obtained showed numerous of rupture events where this continuously increasing loading rate was not observed. Figure 5.5 presents some examples of such curves. This behaviour have impacts on the DFS obtained.

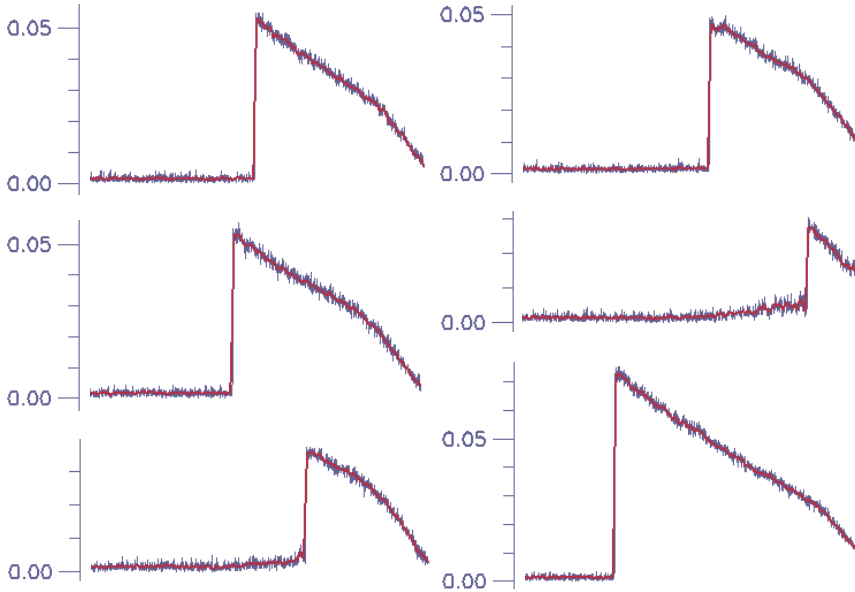


Figure 5.5: Examples of interaction curves with non-exponentially increasing loading rate.

5.6 DF-spectrum of MUC1(ST)-Gal3 interactions

On the basis of calculated rupture force and loading rate from 1036 interactions in the iNanoTrackerOT3-software, the DF-spectrum presented in figure 5.6 was obtained. The different colours in the plot show the subgroups where the rupture forces within a certain loading rate range are grouped together. Figure 5.8 show the result from the Bell-Evans plot to each subgroup, where the f^* -value and r_f (loading rate) to each plot is presented. The DF-spectrum and the subgroups show an exponential increase in loading rate, with a range in f^* -value of 11-31 pN between a r_f -value of 39-72 pN/s. The peak for some of the subgroups a peak could not be identified. Figure 5.8 presents the Bell-Evans plots where the peak could be identified. All Bell-Evans plots are presented in appendix B.

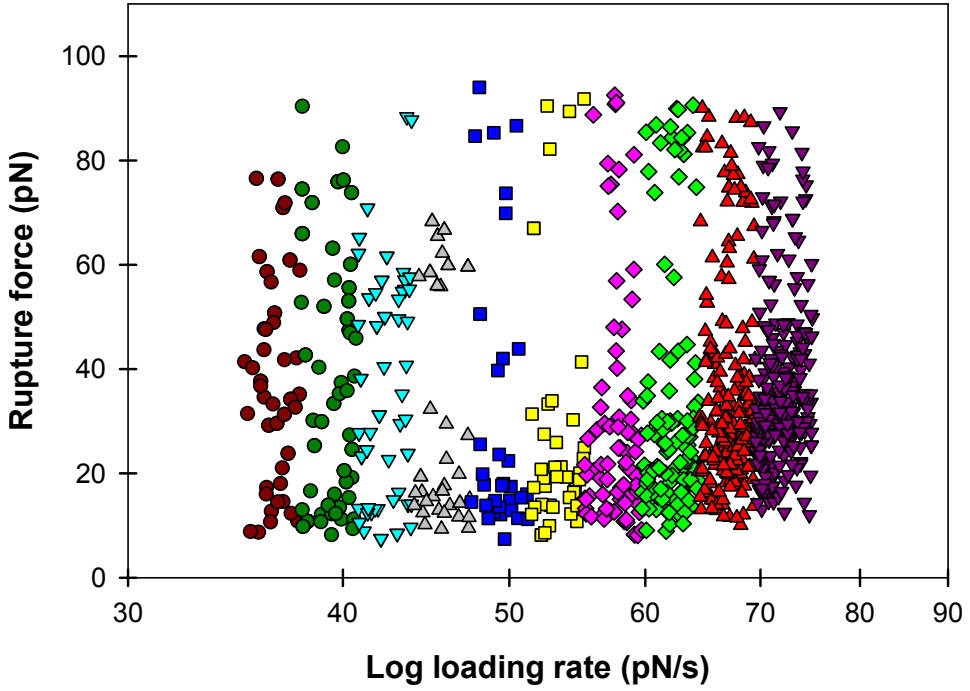
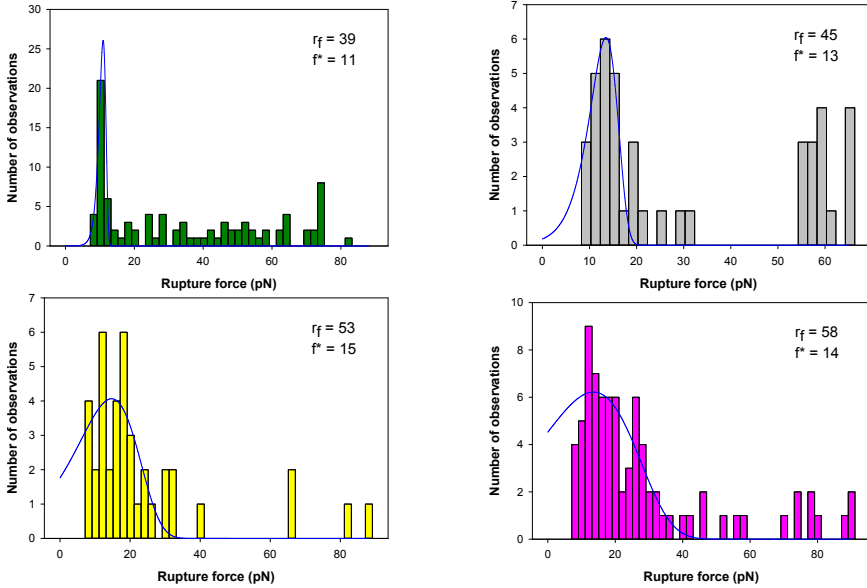


Figure 5.6: DF-spectrum for interactions achieved between MUC1(ST) and Gal3, where log to loading rate on x-axis and rupture force on y-axis is used. The loading rate and rupture force from the interactions are conducted from the iNanoTrackerOT3-software. The plot are divided into subgroups on the basis of rupture force, illustrated with different colours in the plot.



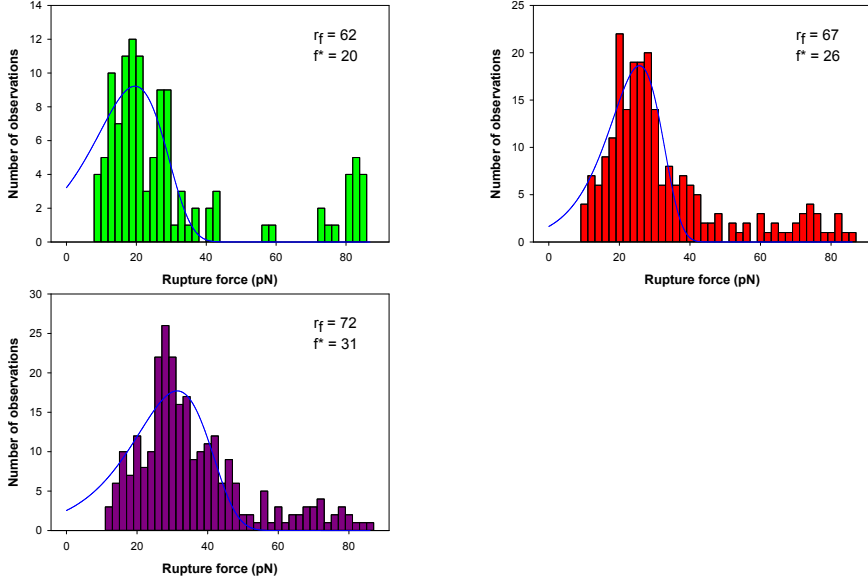


Figure 5.8: Bell-Evans plots of the different subgroups from the DF-spectrum. Each plot is brought up by the number of observations on the y-axis, and the rupture force on the x-axis. The colour to the plots correspond to the same colours presented in figure 5.6. The f^* -value and r_f to each plot is presented in the right corner to all subfigures. The blue line inn all subfigures illustrate the determination of the peak.

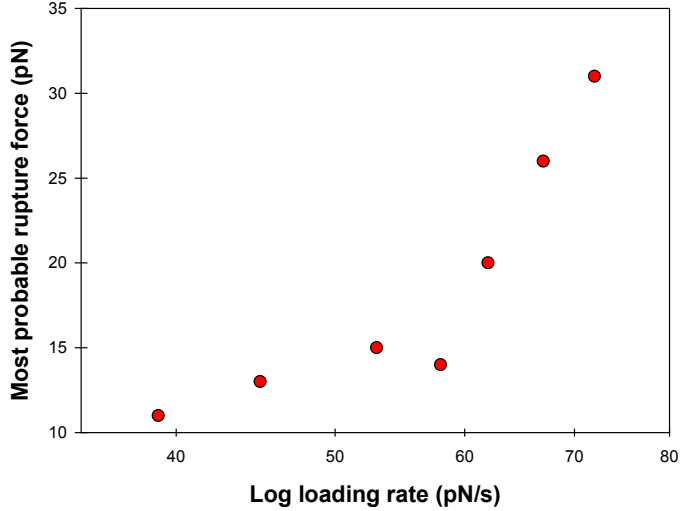


Figure 5.9: Result of the mean trend to the DFS-plot. The mean f^* -value and r_f to each subgroup from figure 5.8 are plotted in a new DFS-plot.

Based on the plots presented in figure 5.8, the mean f^* -value and r_f of each subgroup were identified. These mean values are presented in a separate DFS plot

(figure 5.9). This plot indicate a change in slope, two linear regions can be identified more precisely.

The final results and estimated parameters from figure 5.6, 5.8 and 5.9 are presented in table 5.2. The table present the different subgroups and the number of observations, the r_f , k_{off} , x_β and f^* - values to each subgroup. As described in chapter 3, the k_{off} and x_β are calculated from equation 3.16 and 3.17, but can also be found from the slope of the mean trend in figure 5.9.

Table 5.2: Estimated parameters characterizing the energy landscape of MUC1(ST)-Gal3 interactions.

Interval	Number of observations	r_f (pN/s)	k_{off} (1/s)	x_β (nm)	f^* (pN)
1	58	37	1.5	0.54	-
2	94	39	2.1	0.54	11
3	72	42	2.1	0.54	-
4	44	45	1.3	0.54	13
5	36	49	1.1	0.54	-
6	42	53	2.9	0.067	15
7	81	58	2.5	0.067	14
8	120	62	2.3	0.067	20
9	226	67	1.6	0.067	26
10	263	72	1.3	0.067	31

5.6.1 Non-exponentially increasing loading rate affecting the DF-spectrum

The previous analysis was performed from a dataset with an incubation concentration of MUC1(ST) of 0.10 mg/mL and 0.01 mg/mL of Gal3. The same analysis with an higher incubation concentration of MUC1(ST) and Gal3 (0.15 mg/mL and 0.02 mg/mL) resulted in a increased amount of rupture forces above 100 pN. By further increasing the incubation concentration of MUC1(ST) and Gal3 to 0.30 mg/mL and 0.02 mg/mL, the number of rupture forces above 100 pN decreased but almost all of the interaction curves shown the same non-exponentially increasing loading rate as shown with examples in figure 5.5. Figure 5.10 show a DFS-plot

from the dataset with 0.10 mg/mL MUC1(ST) concentration and 0.01 mg/mL Gal3 concentration (figure 5.10a), 0.15 mg/mL MUC1(ST) concentration and 0.02 mg/mL Gal3 concentration (figure 5.10b), 0.30 mg/mL MUC1(ST) concentration and 0.02 mg/mL Gal3 concentration (figure 5.10c) and all datasets in a combined DFS-plot (figure 5.10d).

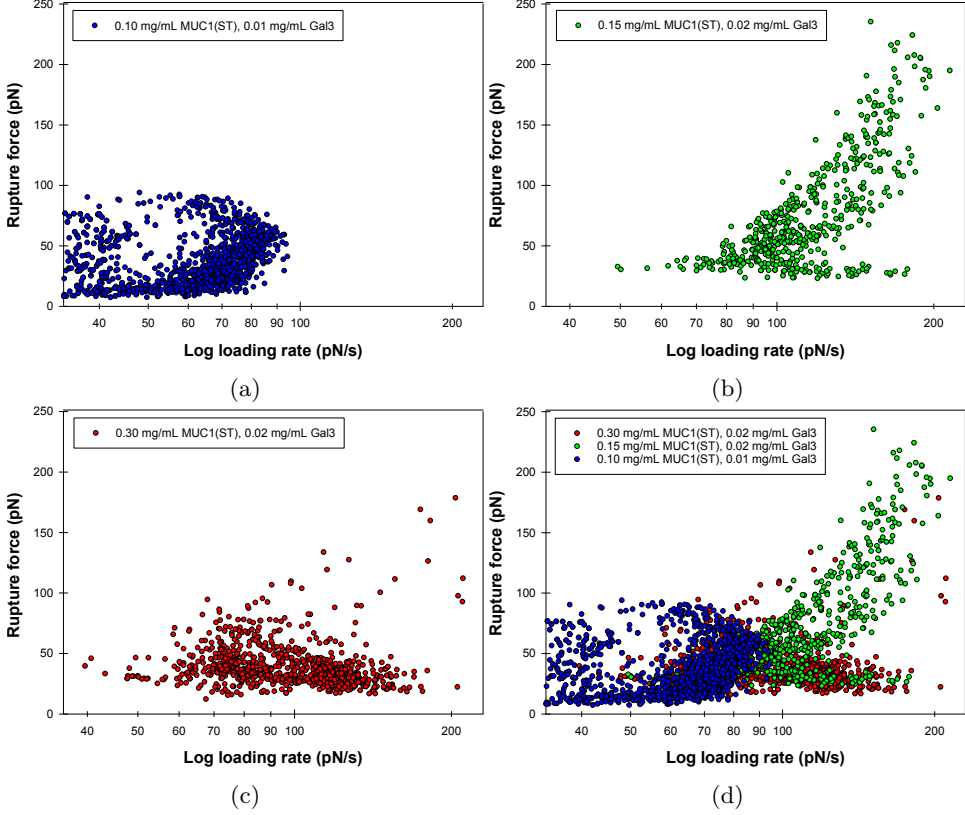


Figure 5.10: Illustration of the results of non-exponentially increasing loading rate affecting the DF-spectrum. All data from interactions between MUC1(ST) and Gal3 with three different incubation concentrations of MUC1(ST) and Gal3 are plotted in each separate DF-spectrum and in one combined DF-spectrum.

Chapter 6

Discussion

This master thesis presents evidence that the OT dual beam set-up is well suited in order to investigate specific glycan-lectin interactions. The experimental data obtained allowed parameters of the energy landscape to be determined, but with regard to some level of inaccuracy. This chapter presents a discussion of the results based on current knowledge in chemistry, biology and physics. The findings are compared with recent publications, and the chapter round off with some thoughts about the non-exponentially increasing loading rate interaction curves observed during analysis.

6.1 How does Gal3 interact with MUC1(ST)?

Galectins are a family of lectins defined by their ability to bind to galactose(Gal)-residues. The evidence presented in this thesis show that the galectin Gal3 binds the two tumor-associated MUC1-antigens ST and T. As described, the ST- and T-structures differ in the manner of sialic acid Neu5Ac content as illustrated in figure 6.1. The structure conformations can be observed in a upscaled figure in the appendix A. This study give rise to an debate during the correctness of the name Gal3 in which the name should include the ability to bind sialic acids. In that manner this study indicate an origin of a new group of lectins, which name could be sialogalectins.

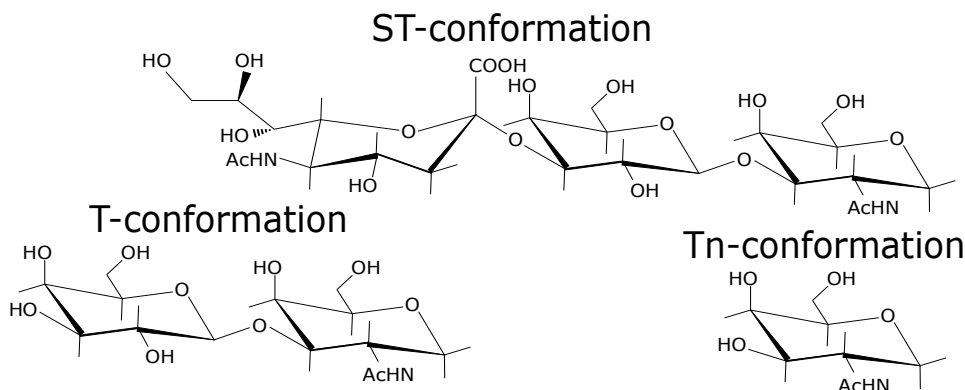


Figure 6.1: ST, T and Tn-antigen structure conformations. The ST-antigen has a α -Neu5Ac(2,3) β -Gal(1,3)-GalNAc-Ser/Thr-conformation, the T-antigen has a β -Gal(1,3)-GalNAc-Ser/Thr-conformation and the Tn-antigen has a GalNAc-Ser/Thr-conformation

The detailed identification of interacting groups on the T-antigen and Gal3 has not yet been performed. However, the interaction are investigated in (Bian et al., 2011) by use of an isothermal titration calorimetry (ITC) assay and surface plasmon resonance (SPR) assay, and in (Rodriguez et al., 2015) by use of an nuclear magnetic resonance spectroscopy (NMR)-instrument. Furthermore, a comparable study has been performed between STn and Tn and the C-type lectin MGL. In this published study information was provided concerning which atoms on each of the two interacting molecules that take part in the formation of the in-

termolecular bond. The analysis was performed by use of a NMR(nuclear magnetic resonance)-instrument, where both the Tn-antigen and STn-antigen were reported to be interacting with MGL. In fact, the study report of a slightly increased binding strength when the sialic acid was attached (Mortezai et al., 2013). However, the interactions were for both the Tn and the STn antigens primarily due to atoms on the GalNAc unit, and not the sialic acid unit. Due to different lectins, a direct comparison can not be performed but the results are indeed interesting. The information about the sialic acid to sometimes be present but not essential in the interaction to a lectin, opens for a possibility of the same to occur in interaction between MUC1(ST) and Gal3. It is not known whether molecules on only Gal are involved in interaction between the T-antigen and Gal3, or a combination of molecules at both Gal and GalNAc. The fact that the Tn-antigen does not interact with Gal3 opens the possibility for e.g. the AcHN at C2 to be of importance in order to block the interaction between the Tn-antigen and Gal3. Further, the results from this study and the ELISA-study performed by Gianfranco Picco, presented in figure 1.1, revealed information about the ST-antigen and Gal3 to interact at a slightly higher frequency than the T-antigen and Gal3, which indicate the sialic acid to promote the interaction. Similar to the (Mortezai et al., 2013)-study, there could be a possibility that the sialic acid does not affect the interaction ability, in which the main binding area to Gal3 could be somewhere at the Gal-structure or a combination of the Gal-GalNAc structure. Instead the sialic acid could be an enhancer for the interaction energy by providing additional binding to Gal3. Figure 6.2 illustrates some of the binding abilities that could be present in the interaction between the ST-antigen and Gal3. Further investigations on this field are required.

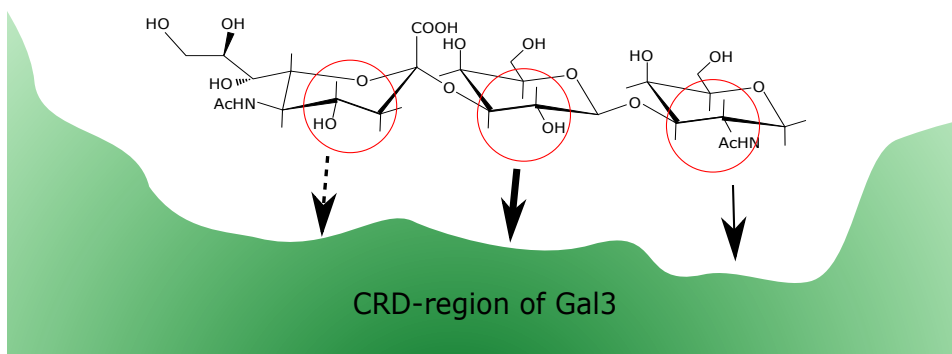


Figure 6.2: Illustration of some binding abilities present in ST-Gal3 interaction. Interactions between the CRD-region at the Gal3 and the ST-antigen could be driven by atoms on the Gal unit, or alternatively the GalNAc unit and/or the Neu5Ac could also contribute.

6.2 Biological consequences of MUC1-Gal3 interactions

The change in MUC1 O-glycosylation to Core-1 antigens has, as described in chapter 2, been reported to have oncogenic consequences such as activation of intracellular pathways, induced metastasis and downregulation of immunerespons by T-cell apoptotis [(Kufe, 2010), (Xin et al., 2015), (Fukumori et al., 2003)]. The main contributor to activation of those pathways is the binding of Gal3 to the Core-1 antigens on MUC1. The presence of the different Core-1 antigens is not fully described, and the percentage of the different MUC1-antigens present in different cancer cells vary. The T-antigen has been reported to be present in 90% of all human carcinomas in (Yu et al., 2007), but the glycan composition has not been analysed. Other articles have reported an increased level of sialic acid on the Core-1 antigens on beast cancers, where the addition of a sialic acid to a T-antigen results in a ST-antigen [(Brockhausen, Yang, Burchell, Whitehouse, & Taylor-Papadimitriou, 1995), (Hanisch, Stadie, Deutzmann, & Peter-Katalinic, 1996), (Lloyd, Burchell, Kudryashov, Yin, & Taylorpapadimitriou, 1996) and (Müller & Hanisch, 2002)]. The findings presented in this master thesis documents the ability of Gal3 to interact not only with MUC1(T) as previously shown but also with MUC1(ST). These new findings thus indicate an increased potential of Gal3 to interact with MUC1 compared to what was previously known. These new findings thus also further emphasize the importance of Gal3 for cancer and its development.

6.3 Glycan specificity of Gal3

6.3.1 Interaction between MUC1(T) and Gal3

The results presented in figure 5.1a, 5.1b and 5.4 as well as table 5.1 show that interaction between MUC1(T) and Gal3 do occur. The narrow peak in the presented histogram (figure 5.1b) shows a relatively high consistence in rupture forces, with few interactions at high forces. Interactions between MUC1(T) and Gal3 is used as a positive control and the findings is in accordance with published articles where the interaction was observed and investigated (Zhao et al., 2010). This consistency between the data obtained using OT and published data obtained using other experimental methods indicates the method to be able to detect glycan-lectin interactions.

6.3.2 Negative control experiments

In order to investigate the reliability of the method, the MUC1(Tn) and MUC1(Na) was used as a negative control samples. There are indications that MUC1(Tn)-antigen does not interact with Gal3 (Iurisci et al., 2000). Furthermore, the MUC1(Na) does not have any glycosylated side chains and therefore can not interact with Gal3. The results obtained for these samples indicated no occurred interactions between MUC1(Tn) and Gal3, or MUC1(Na) and Gal3. The rupture frequency

of 0.5% indicates that interactions occur only in rare cases. The reason why the system identified some rare interactions can be due to the occurrence of unspecific glycan-lectin interactions as described in (Celik & Moy, 2012). The further investigations of interactions between blank polystyrene bead and Gal3 showed some interactions, but in rare cases compared to the positive MUC1(T) control. The rupture frequency determined when allowing blank polystyrene bead to interact with MUC1(ST) was set to 0.0% since the rupture events were rare and due to their abnormal behaviour were impossible to analyse. The few interaction events observed resulted in so high rupture force that the dual beam was not able to separate the beads afterwards. This behaviour might be due to occurrence of ionic forces between the bead surface and the MUC1(ST) molecule, since the polystyrene bead are functionalized with a carboxyl- or a amin-group and the ST-antigen structure consist of a charged sialic acid molecule. The MUC1(Tn)-molecule showed no such events as observed for the MUC1(ST) during investigations of interactions to the same polystyrene bead, but some interactions similar to the blank polystyrene bead against Gal3 was detected. The Tn-antigen structure does not have any charged sialic acid units, which strengthen the theory of ionic forces between the MUC1(ST)-molecule and the blank polystyrene bead. The 7.8 % rupture frequency observed for the blank polystyrene bead and MUC1(Tn) interaction indicates occurrence of some interactions, but these are considered as unspecific interactions due to the negative interaction results between MUC1(Tn) and Gal3. The overall conclusion that can be drawn based on the negative controls is that the specificity and reliability of the method is acceptable, and it is thus a powerful method for investigations of interactions between MUC1(ST) and Gal3.

6.3.3 Interaction between MUC1(ST) and Gal3

The results from the histogram (figure 5.2b) and the rupture frequency analysis (figure 5.4 and table 5.1) show that interaction between MUC1(ST) and Gal3 occur. The positive and negative control analysis indicates that Gal3 forms specific interaction with MUC1(T) and MUC1(ST). The rupture frequency of 42.8 % show a higher interaction frequency for Gal3 when interacting with MUC1(ST) compared to interactions between MUC1(T) and Gal3. Further, the SD value of 26 indicate a large spread in interaction frequency, which introduces an uncertainty to the specific value. The observations of interactions with a rupture strength above 100 pN indicates the system to be more reactive than for the interaction between MUC1(T) and Gal3. The concentration of the two molecules during bead incubation does affect the histogram analysis, where the data in the histogram for MUC1(ST) and Gal3 was with a incubation concentration of 0.10-0.30 mg/mL with MUC1(ST) and 0.01-0.02 mg/mL with Gal3. In order to compare, the data in the histogram for MUC1(T) and Gal3 was with a incubation concentration of 0.17 mg/mL with MUC1(T) and 0.02 mg/mL with Gal3. The incubation concentration of the two systems are considered as almost equal, where an comparison can be performed on a general level.

The MUC1 sample were prepared by collaborators at the oncology department at Kings Collages in London. The MUC1(ST) sample is prepared by removing the

sialic acid from the MUC1(T)-sample. The result of the production of MUC1(ST) is that the MUC1(ST)-sample contain about 1% of MUC1(T)(Ref. Gianfranco Picco, personal communication). Based on the results, a reduction of high interaction forces should be observed for the MUC1(ST)-Gal3 interactions if Gal3 only can interact with MUC1(T). Instead, the opposite behaviour is detected, where the MUC1(T) have a lower probability for high rupture forces compared to what is observed for MUC1(ST) when interacting with Gal3.

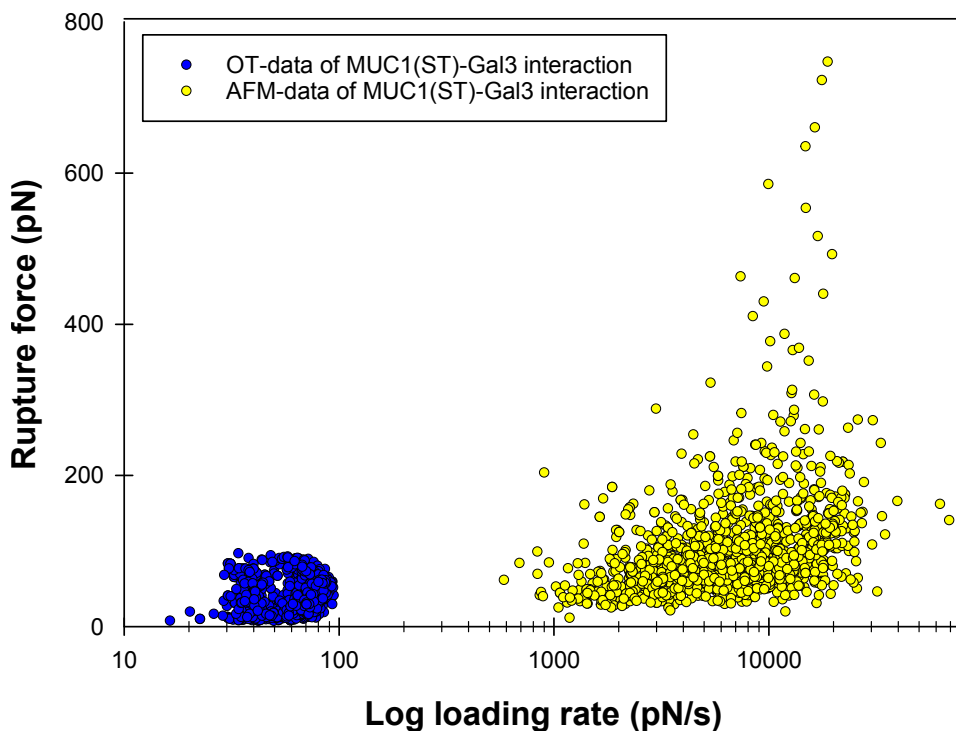


Figure 6.3: Combined DF-spectrum for MUC1(ST) and Gal3 measured analysed in AFM and OT, where log to loading rate on x-axis and rupture force on y-axis is used.

The findings from (Yu et al., 2007), where interaction was reported to not occur between MUC1(ST) and Gal3, are in contrast to the results obtained in this study. Yu and co-workers claim that interaction with Gal3 was only possible when the sialic acid on the ST-antigen structure was removed, resulting in a presence of the T-antigen. To be mentioned is that the study used a western blot-technique, where the interactions are observed at a cellular level and not at a molecular level. Also in contrast to the findings from (Yu et al., 2007), the results from a glycan specific MUC1-Gal3 ELISA-analysis from Gianfranco Picco at King's College London, presented in figure 1.1, show data that are in accordance with the findings obtained in the present study using OT. In the data obtained by Gianfranco Picco the occurrence of MUC1(ST)-Gal3 interactions was at a slightly higher level compared to MUC1(T)-Gal3 interactions. Another master student at NTNU, Ragna Emilie

Bugge, has provided evidence that interaction between MUC1(ST) and Gal3 does occur. Her data were obtained using another sensitive force probe called atomic-force microscopy (AFM). Her data are presented in figure 6.3 where the results from this study and hers are combined in a DFS-plot. The data obtained in OT and AFM show linear correlation. Despite the western blot-results from (Yu et al., 2007), there are weighty evidence that interaction between MUC1(ST) and Gal3 does occur.

6.4 Energy landscape of MUC1(ST)-Gal3 interaction

The DF-spectrum of MUC1(ST)-Gal3 interactions shows a rupture forces with an increase in loading rate, as expected according to chapter 3. Further, the way of determining the loading rate from the shape of the rupture event as implemented in the iNanoTrackerOT3D-software introduces an inaccuracy of the rupture force-loading rate relation, due to variable values of $\frac{\Delta f}{\Delta d}$ which represent the length of the calculated slope. The calculation of the loading rate slope is also based on a logarithmic proportionality between the loading rate and rupture force, in which several interaction curves show a linear proportionality, a decrease in loading rate at increased rupture forces, or a flattening of the loading rate slope at increased rupture forces. This observations is most likely due to presence of multiple interactions. A systematic error of rupture force-loading rate relation will impact the Bell-Evans plots and further the measured r_f , k_{off} , x_β and f^* - values. The two last mentioned curve types can be observed and neglected, but the first are difficult to observe which mean that they are included in the analysis. This uncertainty of the processed values is important to have in mind.

Despite the uncertainty in loading rate determination, the way of using the Bell-Evans plots in figure 5.8 decrease the importance of this error by detecting the peak of the most probable rupture force at a given loading rate. By this, the majority of the interactions at high rupture forces and unnormal loading rate are neglected due to most of the interactions are correct analysed and will do the basis for the peak determination.

The estimated values of r_f , k_{off} , x_β and f^* can further be compared to other studies on glycan-lectin interactions by use of the OT-instrument [(Sletmoen, Dam, Gerken, Stokke, & Brewer, 2009), (Hadjialirezaei et al., 2017)]. The first article (Sletmoen et al., 2009) investigated interactions of the ability of Soybean Agglutinin (SBA) to bind the Tn-antigen on Porcine Submaxillary Mucin (PSM), where the second article (Hadjialirezaei et al., 2017) investigated the ability of C-type lectin MGL to bind MUC1(Tn) or MUC1(STn). The findings from the OT-study (Hadjialirezaei et al., 2017) indicated a MUC1(Tn)-MGL interaction strength (r_f) of 6.8-27.0 pN, a loading rate of 6.8-134 pN/s, k_{off} from 1.5-2.3 s^{-1} and x_β of 0.51 nm. The AFM study to (Sletmoen et al., 2009) indicated a Tn-PSM-SBA interaction strength (r_f) of 103-402 pN, a loading rate of 0.18-266 nN/s, k_{off} from 0.68-31.1 s^{-1} and x_β of 0.05-0.12 nm. Both articles showed that the estimated values of r_f ,

k_{off} , x_β and f^* in this study are in a plausible range for glycan-lectin interactions, which provide credibility to the results obtained.

6.5 Rupture frequency analysis

The rupture frequency analysis was performed in order to distinguish between how frequently an interaction occurred for each molecule-pair. During measurements in the OT-instrument, rare interactions between MUC1(Tn)-Gal3 or MUC1(Na)-Gal3 were observed despite the published article of no interactions indicated between MUC1(Tn) and Gal3 (Iurisci et al., 2000). As explained, these observed rupture events were most likely due to unspecific interactions. In order to separate unspecific interactions and specific interactions, the rupture frequency analysis was performed, in which the results show a distinct difference between the protein complexes that have been found to be interacting (MUC1(T)-Gal3) and the protein complexes that are not found to be interacting (MUC1(Tn)-Gal3 and MUC1(Na)-Gal3).

During measurements, a small drift in the system was observed. This drift resulted in a slightly changed distance between the polystyrene beads. Due to the fact that the distance between the polystyrene beads directly affects the probability for observing an interaction, an interaction event was needed to be observed in order to find the exact distance where interactions are likely to occur. When investigating the probability for bond formation, series of 20 subsequent curves were collected, where the first curve of each set contained a rupture event. Further, the mean rupture frequency was calculated based on five parallel series, each containing 20 curves. The manual procedure used to identify the rupture events constituted a source of uncertainty in the rupture frequency analysis. The standard deviations of each mean rupture frequency value are included in the analysis in order to show the spread behind the mean value. Despite these limitations, the rupture frequency analysis gives an indication of an occurrence of interaction in the complex MUC1(T)-Gal3 and in the complex MUC1(ST)-Gal3.

6.6 Non-exponentially increasing loading rate

The majority of force versus distance curves obtained when using MUC1(ST)-concentration of 0.15-0.30 mg/mL and Gal3-concentration of 0.02 mg/mL showed a clear non-exponentially increasing force prior to the rupture event. The interaction curves obtained when using MUC1(ST)-concentration of 0.10 mg/mL and Gal3-concentration of 0.01 mg/mL showed the expected increase in force with increasing loading rate. The diverging behaviour are most likely due to the influence of multiple interactions since the slope in all the unnormal curves have a point of change at around 27 pN rupture force. A determination of loading rate from such curves results in the plot (b) and (c) in figure 5.10.

One of the possible explanations of the diverging behaviour of the interaction curves could be a type of peeling effect of several ST-antigens on the MUC1-surface

from the Gal3 coated polystyrene beads. This effect has been discussed in an article from 2006, where the study shows and discuss in figure 6 some possible explanations for different rupture curves (Friedsam, Gaub, & Netz, 2006). A single rupture event is found when one interaction is present, but the shape of the rupture curves changes when the number of interactions increases. The investigations were done by use of the AFM-instrument, but the logic behind such events can be compared to the MUC1(ST)-Gal3 complex. Due to the fact that the Gal3-monomer can or will operate in pentamer formations when bound the polystyrene bead, increases the possibility of multiple binding possibilities to the MUC1-glycan structures. The knowledge of 5 glycosylation sites per TR-region in the used samples, and where the MUC1-backbone consist of 16 TR-regions, gives 80 possible binding sites per MUC1-structure. In other words, the possibility of influence by multiple interactions when a interaction is observed are high for the MUC1-Gal3 set-up. During incubation with a MUC1-concentration of 0.30 mg/mL and a Gal3-concentration of 0.02 mg/mL, the protein density on one polystyrene bead or both can be at a so high level that the MUC1-proteins interact with the Gal3-proteins, leading to occurrence of a large amount of interactions at the same time. When the proteins are detached, a high number of rupture events are required in order to separate the polystyrene beads completely. The large amount of rupture events will contribute to the measured impact of a given force per second (loading rate), due to the possibility of a given displacement between each rupture events. The displacement between two rupture events will trick the instrument to measure a lower force per second acting on the beads, and if the concentration of the proteins are at a high level and the following occurred interaction and rupture events are high, the change in displacement between a large number of rupture events can give rise to the diverging behaviour as observed in the results.

Chapter 7

Conclusion

This study present evidence that interactions between MUC1(ST) and Gal3 occur. The measurements were obtained by use of a optical tweezer dual beam setup, in order to study the occurrence of interactions at a molecular level. Rupture events from 11-31 pN was observed with a corresponding loading rate of 39-72 pN/s. The calculated values of the energy landscape gave a k_{off} -range from 1.3-2.9 s^{-1} and x_{β} -values of 0.54 and 0.067 nm. The rupture frequency analysis showed a rupture frequency estimate of $42.8 \% \pm 26$. Interactions between the positive control MUC1(T) and Gal3 gave a rupture frequency estimate of $32.0 \% \pm 16$. The negative controls MUC1(Tn) and MUC1(Na) gave no specific occurrence of interaction with Gal3.

The new findings that this master thesis provide emphasize the importance of Gal3 for cancer and its development. By interacting with both MUC1(ST) and MUC1(T), Gal3 have the ability to interact with a large number of antigen structures on cancer cells, and these interactions result in several tumor-associated signalling events.

Bibliography

- Alberts, B., Wilson, J. H., & Hunt, T. (2015). *Molecular biology of the cell* (6th ed.) [Book]. New York: Garland Science.
- Beatson, R., Maurstad, G., Picco, G., Arulappu, A., Coleman, J., Wandell, H. H., ... Burchell, J. M. (2015). The breast cancer-associated glycoforms of muc1, muc1-tn and sialyl-tn, are expressed in cosmc wild-type cells and bind the c-type lectin mgl [Journal Article]. *PloS one*, 10(5), e0125994. doi: 10.1371/journal.pone.0125994
- Bian, C.-F., Zhang, Y., Sun, H., Li, D.-F., Wang, D.-C., & Lahmann, M. (2011). Structural basis for distinct binding properties of the human galectins to thomsen-friedenreich antigen (gal-3, but not gal-1, recognizes tf antigen) [Journal Article]. *PLoS ONE*, 6(9), e25007. doi: 10.1371/journal.pone.0025007
- Bizzarri, A. R., & Cannistraro, S. (2010). The application of atomic force spectroscopy to the study of biological complexes undergoing a biorecognition process [Journal Article]. *Chem Soc Rev*, 39(2), 734-49. doi: 10.1039/b811426a
- Brockhausen, I. (2006). Mucin-type o-glycans in human colon and breast cancer: glycodynamics and functions [Journal Article]. *EMBO reports*, 7(6), 599-604. doi: 10.1038/sj.embor.7400705
- Brockhausen, I., Yang, J., Burchell, J., Whitehouse, C., & Taylor-Papadimitriou, J. (1995). Mechanisms underlying aberrant glycosylation of muc1 mucin in breast cancer cells [Journal Article]. *European Journal of Biochemistry*, 233(2), 607-617. doi: 10.1111/j.1432-1033.1995.607.2.x
- Burchell, J., Mungul, A., & Taylor-Papadimitriou, J. (2001). O-linked glycosylation in the mammary gland: Changes that occur during malignancy [Journal Article]. *Journal of Mammary Gland Biology and Neoplasia*, 6(3), 355-364. doi: 10.1023/A:1011331809881
- Celik, E., & Moy, V. T. (2012). Nonspecific interactions in afm force spectroscopy measurements [Journal Article]. *Journal of Molecular Recognition*, 25(1), 53-56. doi: 10.1002/jmr.2152
- Chia, J., Goh, G., & Bard, F. (2016). Short o-galnac glycans: regulation and role in tumor development and clinical perspectives [Journal Article]. *Biochimica et Biophysica Acta (BBA) - General Subjects*, 1860(8), 1623-1639. doi: http://doi.org/10.1016/j.bbagen.2016.03.008
- Corfield, A. P. (2015). Mucins: a biologically relevant glycan barrier in mucosal

- protection [Journal Article]. *Biochim Biophys Acta*, 1850(1), 236-52. doi: 10.1016/j.bbagen.2014.05.003
- Di Lella, S., Sundblad, V., Cerliani, J. P., Guardia, C. M., Estrin, D. A., Vasta, G. R., & Rabinovich, G. A. (2011). When galectins recognize glycans: From biochemistry to physiology and back again [Journal Article]. *Biochemistry*, 50(37), 7842-57. doi: 10.1021/bi201121m
- Ding, Z., Lai, G., Sakakibara, T., & Shinohara, S. (2000). Determination of the spring constant of an optical trap by external sinusoidal excitation and lock-in detection [Journal Article]. *Journal of Applied Physics*, 88(2), 737-741. doi: 10.1063/1.373730
- Dudko, O. K., Hummer, G., & Szabo, A. (2008). Theory, analysis, and interpretation of single-molecule force spectroscopy experiments [Journal Article]. *Proceedings of the National Academy of Sciences of the United States of America*, 105(41), 15755-15760. doi: 10.1073/pnas.0806085105
- Evans, E. (1999). Looking inside molecular bonds at biological interfaces with dynamic force spectroscopy [Journal Article]. *Biophysical Chemistry*, 82(2), 83-97. doi: 10.1016/S0301-4622(99)00108-8
- Evans, E., & Ritchie, K. (1997). Dynamic strength of molecular adhesion bonds [Journal Article]. *Biophysical Journal*, 72(4), 1541-1555. doi: 10.1016/S0006-3495(97)78802-7
- Fortuna-Costa, A., Gomes, A. M., Kozlowski, E. O., Stelling, M. P., & Pavão, M. S. G. (2014). Extracellular galectin-3 in tumor progression and metastasis [Journal Article]. *Frontiers in Oncology*, 4(138). doi: 10.3389/fonc.2014.00138
- Friedsam, C., Gaub, H. E., & Netz, R. R. (2006). Probing surfaces with single-polymer atomic force microscope experiments [Journal Article]. *Biointerphases*, 1(1), MR1-MR21. doi: 10.1116/1.2171996
- Fukumori, T., Takenaka, Y., Yoshii, T., Kim, H.-R. C., Hogan, V., Inohara, H., ... Raz, A. (2003). Cd29 and cd7 mediate galectin-3-induced type ii t-cell apoptosis [Journal Article]. *Cancer Research*, 63(23), 8302-8311.
- Hadjilirezaei, S., Picco, G., Beatson, R., Burchell, J., Stokke, B. T., & Sletmoen, M. (2017). Interactions between the breast cancer-associated muc1 mucins and c-type lectin characterized by optical tweezers [Journal Article]. *PLoS One*, 12(4), e0175323. doi: 10.1371/journal.pone.0175323
- Hagisawa, S., Ohyama, C., Takahashi, T., Endoh, M., Moriya, T., Nakayama, J., ... Fukuda, M. (2005). Expression of core 2 beta1,6-n-acetylglucosaminyltransferase facilitates prostate cancer progression [Journal Article]. *Glycobiology*, 15(10), 1016.
- Hanisch, F., Stadie, T. R. E., Deutzmann, F., & Peter-Katalinic, J. (1996). Muc1 glycoforms in breast cancer [Journal Article]. *European Journal of Biochemistry*, 236(1), 318-327. doi: 10.1111/j.1432-1033.1996.00318.x
- Hollingsworth, M. A., & Swanson, B. J. (2004). Mucins in cancer: protection and control of the cell surface [Journal Article]. *Nat Rev Cancer*, 4(1), 45-60. doi: http://www.nature.com/nrc/journal/v4/n1/supinfo/nrc1251_S1.html
- Ibe, O. C. (2013). *Brownian motion* [Book]. Hoboken: Wiley. doi: 10.1002/

9781118618059.ch5

- Iurisci, I., Tinari, N., Natoli, C., Angelucci, D., Cianchetti, E., & Iacobelli, S. (2000). Concentrations of galectin-3 in the sera of normal controls and cancer patients [Journal Article]. *Clinical cancer research: an official journal of the American Association for Cancer Research*, 6(4), 1389.
- Klyosov, A. A., Witczak, Z. J., & Platt, D. (2008). *Galectins* [Book]. Hoboken: Wiley.
- Kondo, K., Kohno, N., Yokoyama, A., & Hiwada, K. (1998). Decreased muc1 expression induces e-cadherin-mediated cell adhesion of breast cancer cell lines [Journal Article]. *Cancer research*, 58(9), 2014.
- Kufe, D. (2010). Oncogenic function of the muc1 receptor subunit in gene regulation [Journal Article]. *Oncogene*, 29(42), 5663-5666.
- Kyewski, B., Suri-Payer, E., & SpringerLink. (2005). *Cd4+cd25+ regulatory t cells : Origin, function and therapeutic potential* [Book]. Springer Berlin Heidelberg.
- Ligtenberg, M. J., Buijs, F., Vos, H. L., & Hilkens, J. (1992). Suppression of cellular aggregation by high levels of episialin [Journal Article]. *Cancer research*, 52(8), 2318.
- Link, T., Bäckström, M., Graham, R., Essers, R., Zörner, K., Gätgens, J., ... Noll, T. (2004). Bioprocess development for the production of a recombinant muc1 fusion protein expressed by cho-k1 cells in protein-free medium [Journal Article]. *Journal of Biotechnology*, 110(1), 51-62. doi: 10.1016/j.jbiotec.2003.12.008
- Lloyd, K., Burchell, J., Kudryashov, V., Yin, B., & Taylorpapadimitriou, J. (1996). Comparison of o-linked carbohydrate chains in muc-1 mucin from normal breast epithelial cell lines and breast carcinoma cell lines - demonstration of simpler and fewer glycan chains in tumor cells [Journal Article]. *J. Biol. Chem.*, 271(52), 33325-33334. doi: 10.1074/jbc.271.52.33325
- Marth, J. D., & Grewal, P. K. (2008). Mammalian glycosylation in immunity [Journal Article]. *Nat Rev Immunol*, 8(11), 874-887.
- Mbanefo, E. C., Kikuchi, M., Huy, N. T., Shuaibu, M. N., Cherif, M. S., Yu, C., ... Hirayama, K. (2014). Characterization of a gene family encoding sea (sea-urchin sperm protein, enterokinase and agrin)-domain proteins with lectin-like and heme-binding properties from schistosoma japonicum [Journal Article]. *PLoS Neglected Tropical Diseases*, 8(1), e2644. doi: 10.1371/journal.pntd.0002644
- Mehul, B., & Hughes, R. C. (1997). Plasma membrane targetting, vesicular budding and release of galectin 3 from the cytoplasm of mammalian cells during secretion [Journal Article]. *J Cell Sci*, 110 (Pt 10), 1169-78.
- Menon, R. P., & Hughes, R. C. (1999). Determinants in the n-terminal domains of galectin-3 for secretion by a novel pathway circumventing the endoplasmic reticulum-golgi complex [Journal Article]. *Eur J Biochem*, 264(2), 569-76.
- Müller, S., & Hanisch, F.-G. (2002). Recombinant muc1 probe authentically reflects cell-specific o-glycosylation profiles of endogenous breast cancer mucin. high density and prevalent core 2-based glycosylation [Journal Article]. *Journal of*

- Biological Chemistry*, 277(29), 26103-26112. doi: 10.1074/jbc.M202921200
- Mori, Y., Akita, K., Yashiro, M., Sawada, T., Hirakawa, K., Murata, T., & Nakada, H. (2015). Binding of galectin-3, a β -galactoside-binding lectin, to muc1 protein enhances phosphorylation of extracellular signal-regulated kinase 1/2 (erk1/2) and akt, promoting tumor cell malignancy [Journal Article]. *The Journal of biological chemistry*, 290(43), 26125. doi: 10.1074/jbc.M115.651489
- Moriyama, H., Nakano, H., Igawa, M., & Nihira, H. (1987). T antigen expression in benign hyperplasia and adenocarcinoma of the prostate [Journal Article]. *Urol Int*, 42(2), 120-3.
- Mortezai, N., Behnken, H. N., Kurze, A.-K., Ludewig, P., Buck, F., Meyer, B., & Wagener, C. (2013). Tumor-associated neu5ac-tn and neu5gc-tn antigens bind to c-type lectin clec10a (cd301, mgl) [Journal Article]. *Glycobiology*, 23(7), 844-852. doi: 10.1093/glycob/cwt021
- Ono, M., & Hakomori, S. (2003). Glycosylation defining cancer cell motility and invasiveness [Journal Article]. *Official Journal of the International Glycoconjugate Organization*, 20(1), 71-78. doi: 10.1023/B:GLYC.0000018019.22070.7d
- Preston, R. J. S., Rawley, O., Gleeson, E. M., & O'Donnell, J. S. (2013). Elucidating the role of carbohydrate determinants in regulating hemostasis: insights and opportunities [Journal Article]. *Blood*, 121(19), 3801-3810. doi: 10.1182/blood-2012-10-415000
- Rodriguez, M. C., Yegorova, S., Pitteloud, J.-P., Chavarroche, A. E., André, S., Ardá, A., ... Cudic, M. (2015). Thermodynamic switch in binding of adhesion/growth regulatory human galectin-3 to tumor-associated tf antigen (cd176) and muc1 glycopeptides [Journal Article]. *Biochemistry*, 54(29), 4462. doi: 10.1021/acs.biochem.5b00555
- Ruvolo, P. P. (2015). Galectin 3 as a guardian of the tumor microenvironment [Journal Article]. *BBA - Molecular Cell Research*, 1863(3), 427-437. doi: 10.1016/j.bbamcr.2015.08.008
- Schwab, M. (2012). Muc1 [Book Section]. In *Encyclopedia of cancer* (p. 2384-2386). Springer Berlin Heidelberg.
- Sharon, N., & Lis, H. (2007). *Lectins* [Book]. Dordrecht: Springer Netherlands: Dordrecht. doi: 10.1007/978-1-4020-6953-6
- Sletmoen, M., Dam, T. K., Gerken, T. A., Stokke, B. T., & Brewer, C. F. (2009). Single-molecule pair studies of the interactions of the α -galnac (tn-antigen) form of porcine submaxillary mucin with soybean agglutinin [Journal Article]. *Biopolymers*, 91(9), 719-728. doi: 10.1002/bip.21213
- Song, K., Herzog, B. H., Fu, J., Sheng, M., Bergstrom, K., McDaniel, J. M., ... Xia, L. (2015). Loss of core 1-derived o-glycans decreases breast cancer development in mice [Journal Article]. *The Journal of biological chemistry*, 290(33), 20159. doi: 10.1074/jbc.M115.654483
- Sulchek, T., Friddle, R. W., & Noy, A. (2006). Strength of multiple parallel biological bonds [Journal Article]. *Biophysical Journal*, 90(12), 4686-4691. doi: 10.1529/biophysj.105.080291

- Wesseling, J., Van Der Valk, S. W., & Hilkens, J. (1996). A mechanism for inhibition of e-cadherin-mediated cell-cell adhesion by the membrane-associated mucin episialin/muc1 [Journal Article]. *Molecular Biology of the Cell*, 7(4), 565-577.
- Xin, M., Dong, X., & Guo, X. L. (2015). Role of the interaction between galectin-3 and cell adhesion molecules in cancer metastasis [Journal Article]. *Biomed. Pharmacother.*, 69, 179-185. doi: 10.1016/j.biopha.2014.11.024
- Yu, L.-G. (2007). The oncofetal thomsen–friedenreich carbohydrate antigen in cancer progression [Journal Article]. *Glycoconjugate Journal*, 24(8), 411-420. doi: 10.1007/s10719-007-9034-3
- Yu, L.-G., Andrews, N., Zhao, Q., McKean, D., Williams, J. F., Connor, L. J., ... Rhodes, J. M. (2007). Galectin-3 interaction with thomsen-friedenreich disaccharide on cancer-associated muc1 causes increased cancer cell endothelial adhesion [Journal Article]. *The Journal of Biological Chemistry*, 282(1), 773-781.
- Zhao, Q., Barclay, M., Guo, X., Barrow, H., Rhodes, J. M., Yu, L.-G., & Hilkens, J. (2010). Interaction between circulating galectin-3 and cancer-associated muc1 enhances tumour cell homotypic aggregation and prevents anoikis [Journal Article]. *Molecular Cancer*, 9. doi: 10.1186/1476-4598-9-154

Appendices

Appendix A

ST, T and Tn-antigen structure conformations

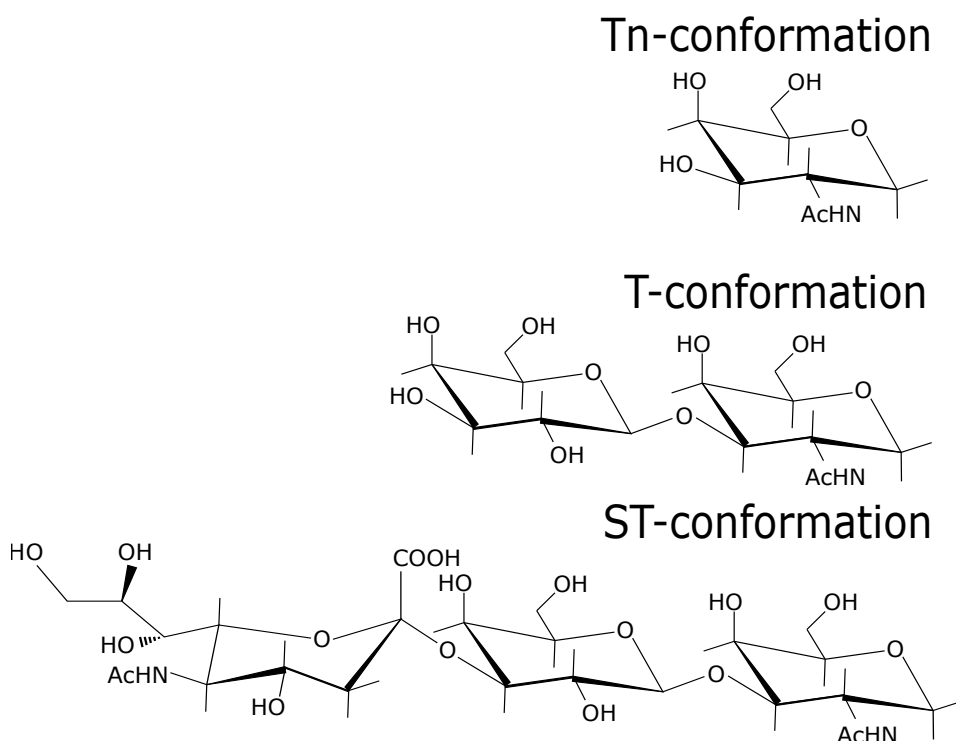


Figure A.1: ST, T and Tn-antigen structure conformations. The ST-antigen has a α -Neu5Ac(2,3) β -Gal(1,3)-GalNAc-Ser/Thr-conformation, the T-antigen has a β -Gal(1,3)-GalNAc-Ser/Thr-conformation and the Tn-antigen has a GalNAc-Ser/Thr-conformation

Appendix B

Histogram results of MUC1(ST)-Gal3 interactions

From the DF-spectrum presents in figure 5.6 and duplicated in B.1, a number of 10 Bell-Evans plots were chosen. The peak determination was not possible for all the histograms, where those histograms were excluded in chapter 5. All 10 Bell-Evans plots with the peak determination are presented in figure B.2 and B.3.

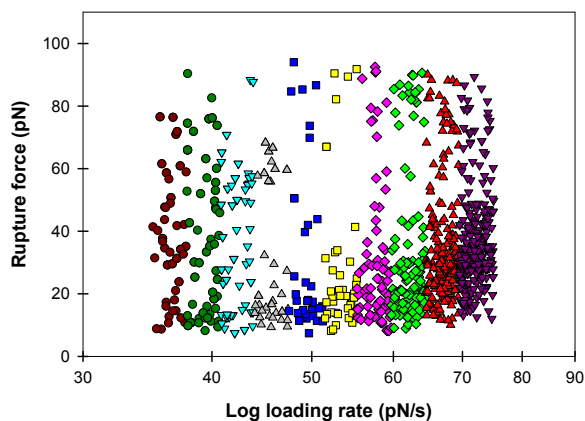
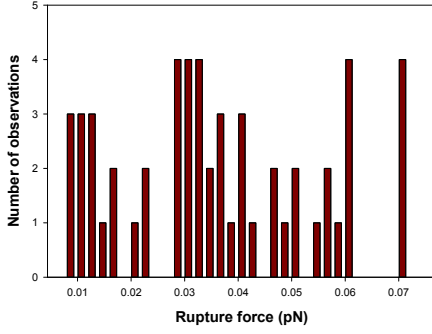
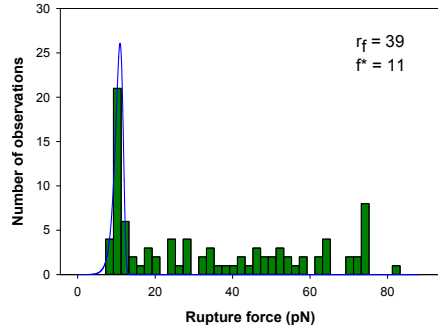


Figure B.1: DF-spectrum for interactions achieved between MUC1(ST) and Gal3, where log to loading rate on x-axis and rupture force on y-axis is used. The loading rate and rupture force from the interactions are conducted from the iNanoTrackerOT3-software. The plot are divided into subgroups on the basis of rupture force, illustrated with different colours in the plot.

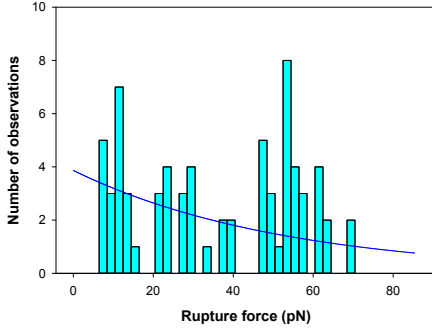
APPENDIX B. HISTOGRAM RESULTS OF MUC1(ST)-GAL3 INTERACTIONS



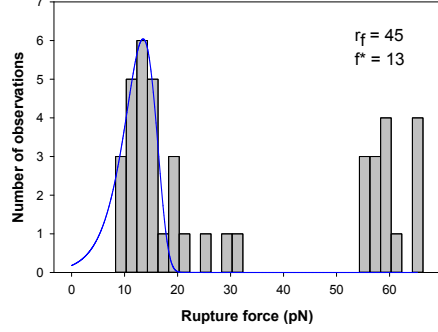
(a) Histogram 1



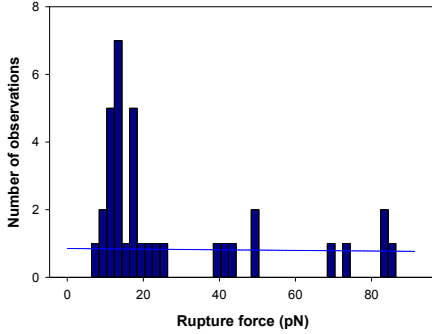
(b) Histogram 2



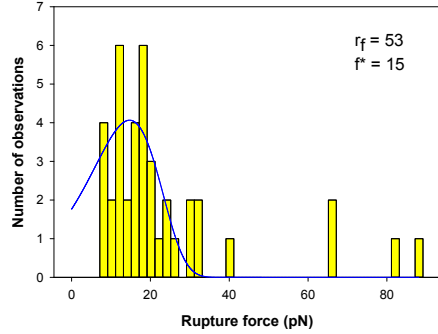
(c) Histogram 3



(d) Histogram 4



(e) Histogram 5



(f) Histogram 6

Figure B.2: Bell-Evans plots of subgroup 1-6 from the DF-spectrum. Each plot is brought up by the number of observations on the y-axis, and the rupture force on the x-axis. The colour to the plots correspond to the same colours presented in figure B.1. The f^* -value and r_f to each plot is presented in the right corner to all subfigures. The blue line inn all subfigures illustrate the determination of the peak.

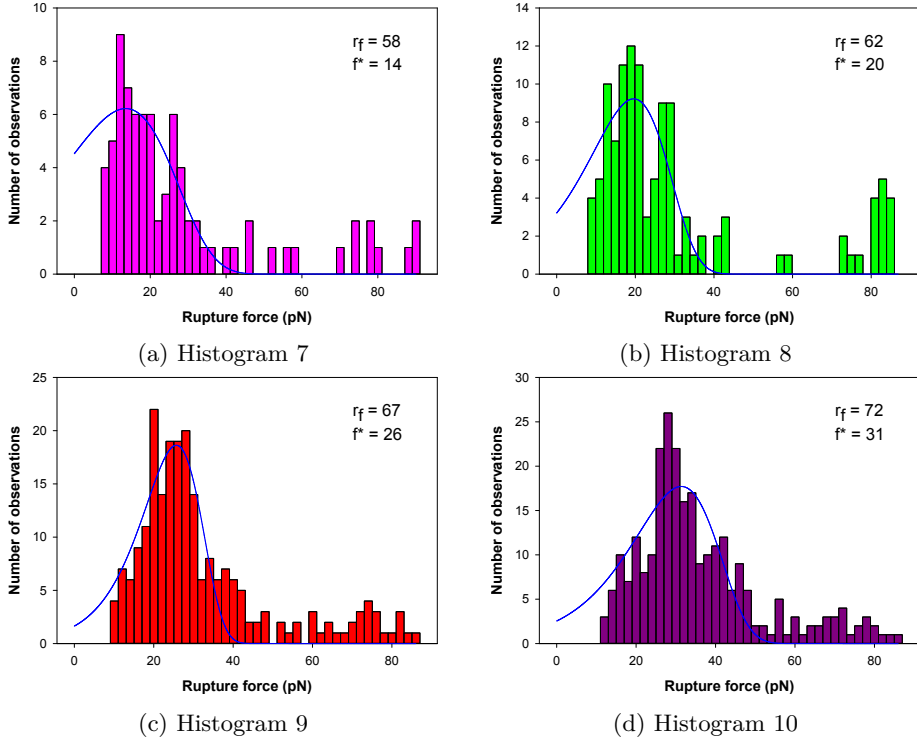


Figure B.3: Bell-Evans plots of subgroup 7-10 from the DF-spectrum. Each plot is brought up by the number of observations on the y-axis, and the rupture force on the x-axis. The colour to the plots correspond to the same colours presented in figure B.1. The f^* -value and r_f to each plot is presented in the right corner to all subfigures. The blue line inn all subfigures illustrate the determination of the peak.

